Probing multiphase gas in local massive elliptical galaxies via multiwavelength observations

Temi, P.; Gaspari, M.; Brighenti, F.; Werner, N.; Grossova, R.; Gitti, M.; ... ; Simionescu, A.

The Astrophysical Journal, 928:150 (22pp), 2022 April 1 https://doi.org/10.3847/1538-4357/ac5036

Probing Multiphase Gas in Local Massive Elliptical Galaxies via Multiwavelength Observations

P. Temi[1], M. Gaspari[2,3], F. Brighenti[4], N. Werner[5], R. Grossova[5], M. Gitti[4,6], M. Sun[7], A. Amblard[1,8], and A. Simionescu[9,10,11]

[1] Astrophysics Branch, NASA—Ames Research Center, MS 245-6, Moffett Field, CA 94035, USA
[2] INAF, Osservatorio di Astrofisica e Scienza dello Spazio, via Pietro Gobetti 93/3, I-40129 Bologna, Italy
[3] Department of Astrophysical Sciences, Princeton University, 4 Ivy Lane, Princeton, NJ 08544-1001, USA
[4] Dipartimento di Fisica e Astronomia, Universitá di Bologna, via Gobetti 93, I-40127 Bologna, Italy
[5] Department of Theoretical Physics and Astrophysics, Faculty of Science, Masaryk University, Kotlářská 2, Brno, 611 37, Czech Republic
[6] INAF, Istituto di Radioastronomia, via Piero Gobetti 101, I-40129 Bologna, Italy
[7] Physics Department, University of Alabama in Huntsville, Huntsville, AL 35899, USA
[8] Carl Sagan Center, SETI Institute, 189 Bernardo Avenue, Mountain View, CA 94043, USA
[9] SRON Netherlands Institute for Space Research, Niels Bohrweg 4, 2333 CA Leiden, The Netherlands
[10] Leiden Observatory, Leiden University, P.O. Box 9513, 2300 RA Leiden, The Netherlands
[11] Kavli Institute for the Physics and Mathematics of the Universe (WPI), The University of Tokyo, Kashiwa, Chiba 277-8583, Japan
Received 2021 November 18; revised 2022 January 14; accepted 2022 January 20; published 2022 April 4

Abstract

We investigate the cold and warm gas content, kinematics, and spatial distribution of six local massive elliptical galaxies to probe the origin of the multiphase gas in their atmospheres. We report new observations, including Stratospheric Observatory for Infrared Astronomy [C II], Atacama Large Millimeter/submillimeter Array CO, Multi Unit Spectroscopic Explorer (MUSE) Hα+[N II], and Very Large Array (VLA) radio observations. These are complemented by a large suite of multiwavelength archival data sets, including thermodynamical properties of the hot gas and radio jets, which are leveraged to investigate the role of active galactic nucleus (AGN) feeding/feedback in regulating the multiphase gas content. Our galactic sample shows a significant diversity in cool gas content, spanning filamentary and rotating structures. In our noncentral galaxies, the distribution of such gas is often concentrated, at variance with the more extended features observed in central galaxies. Misalignment between the multiphase gas and stars suggest that stellar mass loss is not the primary driver. A fraction of the cool gas might be acquired via galaxy interactions, but we do not find quantitative evidence of mergers in most of our systems. Instead, key evidence supports the origin via condensation out of the diffuse halo. Comparing with chaotic cold accretion (CCA) simulations, we find that our cool gas-free galaxies are likely in the overheated phase of the self-regulated AGN cycle, while for our galaxies with cool gas, the k-plot and AGN power correlation corroborate the phase of CCA feeding in which the condensation rain is triggering more vigorous AGN heating. The related C-ratio further shows that central/noncentral galaxies are expected to generate an extended/inner rain, consistent with our sample.

Key words: Elliptical galaxies – Interstellar medium – Active galactic nuclei – Infrared astronomy – Optical astronomy – Radio astronomy – X-ray astronomy

1. Introduction

The cold/warm phase of the interstellar medium (ISM) in elliptical galaxies, although not as massive as in spirals, plays a key role in many, poorly understood physical processes, which control the evolution of these objects. The presence, distribution, and dynamics of the cold gas constrain the nature of the residual star formation in these galaxies, as well as the quenching mechanism and the black hole (BH) accretion −active galactic nucleus (AGN) feedback cycle.

Without an appropriate feedback mechanism (driven by AGN activity, star formation, or both), massive galaxies would grow to even larger stellar masses and undergo intense star formation that would make these galaxies much bluer than they are (e.g., Bower et al. 2006; Croton et al. 2006). AGNs inject huge amounts of energy in the surrounding ISM in both radiative and mechanical form. Their impact on the host galaxies is demonstrated by the various type of outflows, now commonly detected in AGN hosts (e.g., McNamara & Nulsen 2007; King & Pounds 2015, and references therein). Despite the strong negative feedback provided by the AGN, several studies of UV-optical colors indicate that a significant fraction (∼30%) of the local early-type galaxies (ETGs) show evidence of star formation (Kaviraj et al. 2007; Sheen et al. 2016). The origin of the cold gas necessary to form stars is a matter of debate. While minor mergers could trigger some of the star formation activity, internal sources of neutral/molecular material, like stellar mass loss or hot gas cooling, may well dominate the cold gas budget in ellipticals (Lagos et al. 2014; Valentini & Brighenti 2015; Sheen et al. 2016). To understand the critical role of hot gas cooling in the AGN feedback, information on the ISM cold gas phases becomes critical.

Atacama Large Millimeter/submillimeter Array (ALMA) observations have detected CO emission and absorption in massive elliptical galaxies at the center of X-ray bright groups (David et al. 2014; Temi et al. 2018; Rose et al. 2019; Maccagni et al. 2021; North et al. 2021). For the archetypal

group NGC 5044, the CO observations suggest that the molecular gas is indeed distributed in several clouds apparently orbiting within ∼2 kpc from the center. However, the [C II] image of the NGC 5044 core appears smoother and more extended than expected from the small number of discrete CO clouds, suggesting that some diffuse CO was resolved out by ALMA. Colder molecular gas, possibly associated with [C II] emission from photodissociation regions, is also a common presence in central ellipticals (Werner et al. 2014).

Hα emission is regularly detected in massive ellipticals (e.g., Caon et al. 2000; Sarzi et al. 2013; Werner et al. 2014) and probes warm $T \sim 10^4$ K gas, likely photoionized by UV radiation from post-asymptotic-giant-branch stars. The warm gas typically occupies a kinematically irregular region several kiloparsecs in size. One important feature observed in some, group-centered, massive ellipticals (Werner et al. 2014) is the correspondence between the cold molecular gas and the warm ionized phase. Such a co-spatial correlation of different phases can be understood in the multiphase cooling scenario (Valentini & Brighenti 2015; Gaspari et al. 2018) if cooled clouds are characterized by inner layers of colder gas surrounded by an outer warmer skin made photoionized by various local sources (e.g., Mathews & Brighenti 1999; Valentini & Brighenti 2015; Gaspari et al. 2017).

While a significant fraction of the cold gas mass in low-to-intermediate-mass ETGs is thought to have an external, merger-related origin (e.g., Davis et al. 2011, 2019), in the most massive ETGs, of interest here, the cold gas phases are presumably generated internally by cooling (Davis et al. 2011; David et al. 2014; Werner et al. 2014).

In this paper we present new far-infrared (FIR) [C II] observations of a sample of six local massive elliptical galaxies taken with the Field-Imaging Far-Infrared Line Spectrometer (FIFI-LS) on board the Stratospheric Observatory for Infrared Astronomy (SOFIA; Young et al. 2012; Temi et al. 2014). The recently acquired SOFIA data are complemented with a large suite of multiwavelength observations available in the literature, which include, radio (ALMA, Institut de Radioastronomie Millimétrique (IRAM), Very Large Array (VLA)), optical (Hubble Space Telescope (HST) SOuthern Astrophysical Research Telescope (SOAR), and VIsible Multi-Object Spectrograph (VIMOS)), IR (Spitzer, Herschel), and X-ray (Chandra) data. It is worth noting that, in addition to the new SOFIA observations, some of the data retrieved from public archives have not been published yet, and form a set of original and new observations. We will emphasize in the text any of these occurrences. The paper is organized as follows. In Section 2 we describe the sample, while the data reduction and analysis of the multiwavelength data set are detailed in Section 3. The results for each individual galaxy are presented in Section 4. The discussion and conclusions are presented in Sections 5 and 6, respectively.

2. Sample Description

The goal of the SOFIA FIFI-LS observations was to expand the sample of ETGs observed in the [C II] line with Herschal Photodetector Array Camera and Spectrometer (PACS) by obtaining a complete coverage of the sample of 18 nearby ($d < 100$ Mpc), massive, X-ray bright ETGs, with declinations $\delta > 0$, studied by Dunn et al. (2010). These nearby massive galaxies are the lowest redshift proxies of the more distant cluster cooling cores. We focus on the nearest brightest systems in order to study AGN feedback in the greatest possible detail. The galaxies span a broad range of X-ray morphologies and radio jet powers, making the sample well matched to exploring the parameter space of the radio mode AGN feedback cycle. The sample of Dunn et al. (2010) was derived from a larger catalog of 530 ETGs selected by Beuing et al. (1999) with morphological type $T \leqslant -2$ and considered 90% complete at a magnitude of $B_T = 13.5$ mag. The sample consists of all normal galaxies well representative of elliptical and lenticular galaxies, including galaxies at the centers of clusters and groups. From this initial catalog of optically bright galaxies with X-ray luminosity measurements, all galaxies with 0.1–2.4 keV fluxes $>3 \times 10^{-12}$ erg s^{-1} cm^{-2} and within a distance of 100 Mpc were down selected by Dunn et al. (2010). This is essentially regarded as a complete sample of nearby elliptical galaxies with measured optical, X-ray, and radio properties. SOFIA FIFI-LS observations were obtained for the nearest six out of the 12 proposed galaxies. The six galaxies included here should be regarded as an extension of the earlier work initiated with Herschel PACS and expanded by SOFIA on the investigation of the origin of the cold gas phase in these systems. Since these galaxies have been selected from the original sample of Dunn et al. (2010), the combined sample (Herschel + SOFIA) forms a larger and more statistically significant sample. The complementarity of the two, as well as their differences—Herschel's sample traces systems at the center of groups or clusters, whereas systems in the SOFIA's sample are not central—is discussed throughout the paper. These galaxies are also part of the ATLAS3D catalog (Cappellari et al. 2011), which contains most of the massive ($L_K > 8.2 \times 10^9 L_{\odot,K}$, which translates to $M_* \gtrsim 6 \times 10^9 M_\odot$) ETGs in the northern hemisphere at a distance lower than 42 Mpc.

Table 1 shows general parameters for the sample under investigation.

3. Observations

In this section we introduce the multiwavelength data set available for the galactic sample under investigation, starting with the new SOFIA FIR [C II] observations. While data reduction and analysis is presented in detail for new and unpublished observations, we also briefly summarize the reduction processes and data analysis for archival and publicly available data and refer to the appropriate references in the literature.

3.1. [C II] SOFIA FIFI-LS Observations

The sample of six galaxies was observed by FIFI-LS (Klein et al. 2014; Fischer et al. 2018) on board SOFIA for 10–30 minutes each between 2015 March 12 and October 23 (see Table 2) at an altitude between 12 and 13.5 km, depending on the source. In this paper, we use the red channel centered on the velocity-corrected [C II] line (157.74 μm rest frame) for each galaxy, while the blue channel observed simultaneously the [O III] line (88.356 μm rest frame). The spectrometer comprises 25 ×16 pixels of germanium gallium-doped photoconductors. An integral field unit rearranges the 5 × 5 pixel field of view (FOV; each pixel is 12″ on the sky for the red channel) into 25 × 1 pixels that are dispersed by a diffraction grating into the 25 × 16 detector pixels. At the [C II] wavelength, the spectral resolution is about 250 km s^{-1} ($R \sim 1200$), and the spectral range is about 1500 km s^{-1}. The observations were conducted

Table 1
Galactic Sample Information

Galaxy	cz	D	arcsec pc^{-1}	Type	M_K	log(R_e)	ϵ_e	λ_{Re}	F/S	$F_{H\alpha}$	Ref Hα	log(M_H)
	km s^{-1}	Mpc			mag	arcsec				10^{-13}erg cm^{-2} s^{-1}		$M_\odot$
(1)	(2)	(3)	(4)	(5)	(6)	(7)	(8)	(9)	(10)	(11)	(12)	(13)
NGC 4203	1086	15.1	73	E-S0 (-2.7 ± 0.7)	-23.44	1.47	0.154	0.305	F	0.7	5	7.8 ± 0.1
NGC 4261	2212	31.6	152	E (-4.8 ± 0.4)	-25.18	1.58	0.222	0.085	S	4.1	1,5	7.9 ± 0.1
NGC 4374 (M84)	1017	18.4	89	E (-4.4 ± 1.2)	-25.12	1.72	0.147	0.024	S	3.8	2,5	8.2 ± 0.3
NGC 4406 (M86)	-224	17.1	83	E (-4.8 ± 0.5)	-25.04	1.97	0.211	0.052	S	11.4	2,3	4.7 ± 0.4
NGC 4552 (M89)	344	15.8	76	E (-4.6 ± 0.9)	-24.29	1.53	0.047	0.049	S	2.7	2,4,5,6	5.5 ± 0.1
NGC 4649 (M60)	1110	17.3	84	E (-4.6 ± 0.9)	-25.46	1.82	0.156	0.127	F	2.8	2	4.5 ± 0.1
NGC 4636[a]	938	14.7	71	E (-4.8 ± 0.5)	-24.36	1.95	0.036	0.25	S	2.7	4	6.4 ± 0.1

Note. (1): Galaxy name; (2): velocity from NASA/IPAC Extragalactic Database (NED); (3): distance from Tonry et al. (2001); (4): linear size conversion; (5): galaxy type; type T parameter in brackets from hyperleda; (http://leda.univ-lyon1.fr/) (6): absolute K-band magnitude M_K (Two Micron All Sky Survey keyword k_m_ext) from Cappellari et al. (2011); (7): effective radius R_e from Cappellari et al. (2011); (8, 9, 10): ellipticity, specific stellar angular momentum, fast or slow rotator, respectively (slow if $0.31\sqrt{\epsilon_e}/\lambda_{Re} > 1$) at R_e; (11, 12): Hα+[N II] fluxes and references (1: Gavazzi et al. 2018; 2: Trinchieri & di Serego Alighieri 1991; 3: Kenney et al. 2008; 4: Macchetto et al. 1996; 5: Ho et al. 1997; and 6: Boselli et al. 2022) (13): gas mass estimated using a gas-to-dust ratio of 100 and the dust masses calculated by Amblard et al. (2014) using Spitzer and Herschel fluxes of these galaxies (Temi et al. 2009; Amblard et al. 2014); [a]: added to the sample to present new ALMA CO(3–2) data.

Table 2
SOFIA FIFI-LS Observation Parameters of the Galactic Sample

Galaxy	R.A.$_{tel}$	Decl.$_{tel}$	Exposure (s)	Altitude (ft)	ZA (deg)	MISSION-ID
NGC 4203	$12^h15^m05\overset{s}{.}28$	$+33^d11^m50\overset{s}{.}4$	675.8	43002	64.6	2015-10-23_FI_F250
NGC 4261	$12^h19^m23\overset{s}{.}16$	$+05^d49^m31\overset{s}{.}0$	1658.9	43504	36.1	2015-03-13_FI_F200
NGC 4374	$12^h25^m03\overset{s}{.}72$	$+12^d53^m12\overset{s}{.}8$	952.3	40499	31.5	2015-03-27_FI_F206
NGC 4406	$12^h26^m11\overset{s}{.}76$	$+12^d56^m46\overset{s}{.}0$	952.3	41015	33.5	2015-03-27_FI_F206
NGC 4552	$12^h35^m39\overset{s}{.}84$	$+12^d33^m23\overset{s}{.}0$	1751.0	41018	37.9	2015-03-27_FI_F206
NGC 4649	$12^h43^m40\overset{s}{.}08$	$+11^d33^m10\overset{s}{.}1$	890.9	42998	46.7	2015-03-12_FI_F199

Note. The coordinates (R.A., decl.) represent the position of the center of the telescope (center of the 5×5 pixel array as well), and the altitude and zenith angle (ZA) are the mean values. The exposure represents the on-source time, and total observation duration is general about 2.5 time larger. The MISSION-ID indicates the observation date and the SOFIA flight number.

with two-point symmetric chopping and with nodding in mod match chop style with a standard ABBA nod cadence. The chopping frequency was set to 2 Hz for NGC 4203, NGC 4261, and NGC 4649, and to 5 Hz for NGC 4374, NGC 4406, and NGC 4552. NGC 4203 observations were slightly dithered as well. The data used in this paper have been processed by the FIFI-LS pipeline, which subtracts, chops, and calibrates the wavelength and position, applies a flat correction, and combines grating scans. The pipeline then produces Level 3 data by applying a telluric correction, calibrating the fluxes, correcting the wavelength shifts and resampling the wavelength. At that level, the data is a data cube of dimensions $25 \times N_w \times N_{nod}$, where the first dimension represents the 5×5 pixel FOV, the second dimension represents the spectral channel, and the third dimension represents the number of nods performed during the observations. For NGC 4203, we used Level 4 data, where the data has been spatially resampled and the nods combined since all of the nods do not point at the same location because of the dithering. Level 4 data consists of a data cube of dimensions $N_x \times N_y \times N_w$, where N_x and N_y are the number of resampled spatial pixels ($2''$ pixel for the red channel), and N_w is the number of spectral channels.

3.1.1. [C II] SOFIA FIFI-LS Data Reduction

Following recommendation from SOFIA staff, NGC 4203 data were analyzed using Level 4 products, whereas the rest of the data were analyzed using Level 3, because only NGC 4203 observations were dithered and benefit from the regridding and interpolation that is taking place between Levels 3 and 4.

In order to detect emission lines in NGC 4203 data, the spatial and spectral edges of the cube were first discarded, since the noise level is significantly higher (less sampled), and these areas are more prone to systematic effects. Emission lines are also not expected at the edge of the spectrum nor at the edge of the observed area. In each remaining spectral channel, pixels with a flux in excess of the median flux by at least 4.45 times the median absolute deviation (equivalent to 3σ but with outlier removal) are selected. The selected pixels are clustered spatially and spectrally simultaneously using the density-based spatial clustering of applications with noise (DBSCAN) algorithm implemented in the scikit-learn python library.[12] Three pixels are required in order to define a cluster, and the maximum distance is set to 4; otherwise, all other parameters are set to default.

For each cluster, the brightest pixel is then identified (e.g., red cross in Figure 2 bottom plot) and used as the initial point to fit the spatial distribution of the source with a 2D Gaussian function (e.g., black contours in Figure 2 bottom plot). The fitted Gaussian allows us to measure the extent and position of the source and allows us to normalize the total line flux from the brightest pixel spectrum.

The last step of the analysis of the SOFIA NGC 4203 data is to fit the spectrum of the brightest pixel with a 1D Gaussian function. We chose to fit the brightest pixel instead of integrating over the source extent because of the poor signal-to-noise of the data. The spectra and their fits are presented in the top plots of Figure 2, along with the resulting parameters, and the amplitude has been normalized by the source extent as indicated by the units.

For the five other galaxies, Level 3 data were used. The data were corrected for atmospheric transmission, and all of the observed nods (approximately 30–60) of the 5×5 pixels were grouped together. Each pixel is then processed in the following way. First a background is fitted and removed for each of the observed spectra, using a ridge linear regression on channels away from the central channels (velocity greater than 500 km s^{-1}) where we expect the emission lines but excluding channels on the edges of the spectrum, since they are noisier. A median spectrum is calculated from the observations of the pixels that fall in the central 90th percentile of a first estimate of the median spectrum, and a standard deviation is calculated for each channel of the spectrum.

A 1D Gaussian function is fitted on the median spectrum of each of the 25 pixels. Fitted Gaussians with an absolute velocity below 400 km s^{-1} and a signal-to-noise detection greater than three are selected as emission line candidate. The two candidates obtained through this processing are presented in Figures 5 and 8. Given the sparsity of the spatial sampling (5×5 pixel image), the source is assumed to be smaller than the FIFI-LS beam (the FIFI-LS beam size is used for the flux density normalization).

For NGC 4261, given the width and the shape of the detected [C II] feature, we performed a fit with two Gaussians (Figure 5). The resulting χ^2 decreases significantly (by almost a factor three), and the Bayesian information criterion is reduced by 13.9, which strongly indicates that the two-line model is favored. The velocity shift between the two lines is then 434 km s^{-1}, and the velocity dispersion is similar between the two lines.

3.2. CO Observations

We present new and archival CO observations taken with the 12 m array ALMA interferometer and with the single-dish IRAM 30 m telescope.

[12] https://scikit-learn.org

ALMA Data—Three galaxies in the sample, NGC 4261, NGC 4374, and NGC 4649 have been observed with ALMA. In addition, we present new ALMA CO(3–2) observations of the central group elliptical galaxy NGC 4636. Although this galaxy is not a member of the SOFIA [C II] galactic sample, it has been included here because of the newly acquired CO data. NGC 4636 is part of the galactic sample observed in the [C II] line by the Herschel observatory (Werner et al. 2014).

We utilize ALMA CO(2–1) archival data for NGC 4261 acquired under the ALMA science program 2017.1.00301.S (PI A. Barth; Figure 4). The observations were taken with the 12 m antenna interferometer in a configuration providing 0.″3 angular resolution (maximum recoverable scale, MRSA, 4″) and therefore probe smaller scales than [C II] data. We also use ALMA CO observations of NGC 4374 and NGC 4649 presented in the literature. CO(2–1) emission in NGC 4374 is reported by Boizelle et al. (2017) using the 12 m array configured with a 0.″3 resolution. A null detection is reported for NGC 4649 CO(3–2) from data recorded under the science program 2017.1.00830.S (PI N. Nagar) that have an angular resolution of 0.″12.

NGC 4636 has been observed with ALMA during Cycle 5 (project code: 2015.1.01107.S; PI: A. Simionescu). The ALMA interferometer was configured such that its longest baseline was about 640 m and its shortest baseline about 15 m. This configuration resulted in an angular resolution of about 0.″17 and a maximum recoverable scale of 5.″6. Assuming a distance of 14.7 Mpc for NGC 4636, 0.″17 and 5.″6 correspond to 12 and 399 pc, respectively. All data were taken in the ALMA band 7, one spectral window (spw) was centered around the CO (3–2) line, and three other spws measured the continuum. The data were reduced using the Common Astronomy Software Applications (CASA) software (version 4.7.2; McMullin et al. 2007). The observations achieved a sensitivity of 0.71 mJy beam^{-1} in 10 km s^{-1} spectral windows for a 5322 s on-source time, but no clear CO(3–2) line is detected in the data with a significance greater than 5σ using a similar analysis as in Temi et al. (2018). However a 3.5σ point-like signal can be measured at the location of a CO(2–1) cloud detected in Temi et al. (2018) near the center of the galaxy. The inferred flux density CO(3–2) to CO(2–1) line ratio is between 1.1 and 1.8 for this cloud. The source being unresolved in the CO(3–2) data indicates that its size is smaller than ∼0.″17 (12 pc).

IRAM Data—For NGC 4203, NGC 4406, and NGC 4552, CO(1–0) measurements were obtained with the IRAM 30 m telescope, which has an angular resolution of about 22″ and therefore probes angular scales similar to SOFIA FIFI-LS for the [C II] line.

3.3. Nuclear and Extended Dust

We used archival data from the HST to investigate the presence of dust in the core of each of the galactic samples. In addition, cold dust emission in the extended 1′–2′ region has been probed in the infrared by the Spitzer Space Telescope and the *Herschel Space Telescope*.

3.3.1. Dust Absorption from HST

To estimate the amount and morphology of the dust absorption, we used HST images collected on the Hubble Legacy Archive website[13] in a blue/visible filter (F450W, F547M, F555W depending on the galaxy) and red filter (F814W). These data were observed as part of proposals #5999, #11339, #6094, #5512, #5454/6099, and #6286 with the Wide Field and Planetary Camera 2 and Advanced Camera for Surveys instruments.

The dust absorption on the "blue" filter data was estimated by subtracting a model of the stellar emission. We attempted to calculate the stellar emission model either with a functional form obtained with GALFIT[14] (Peng et al. 2010) or with the python library photutils[15] (Bradley et al. 2019), or with a linear function of the "red" filter assuming that the galaxy spectral energy distribution (SED) does not change much across the galaxy. For GALFIT, we first fitted a single component and increased the complexity up to three components (not including a sky background component). We tried several types of profile (Sérsic, Nuker, Ferrer, etc.) with GALFIT, but our models from the photutils or the "red" filter seem to be closer to the true stellar emission for these galaxies. In the end, we chose a photutils model for NGC 4406 and NGC 4552, and a model estimated from the red filter for the other galaxies.

The dust absorption maps are presented in Section 4 for each individual galaxy in the sample (Figures 1, 3, 6, 8, 9, 10). All galaxies except NGC 4649 show some traces of dust. In these figures, the dust absorption is seen in blue (darker blue indicates stronger absorption), yellow and red indicate excess residual emission to the stellar emission model, while green areas mark regions where the stellar emission model is a good match to the galaxy flux (no absorption, nor additional emission). The excess residual emission can result from foreground sources or mismatch between the model and the galaxy (as seen at the center of NGC 4406 and 4552). When using a red filter as the stellar emission template, an excess residual emission can come from sources that are bluer than the average stellar population as well.

As shown in Figures 1 and 6, NGC 4203 and NGC 4374 have the largest amount of dust with prominent dust lanes, visible in each individual observation. NGC 4261 has a very small (about 1″/150 pc diameter) but dense disk of dust at its center, while NGC 4552 and NGC 4406 have several dust plumes along the radial direction extending out up to 4″/300 pc away from the galaxy center. The NGC 4406 dust image shows some complex residual emission at its center, which could not be modeled with the ellipsoid isophote model of photutils nor with a combination of several sersic or exponential profiles with GALFIT. NGC 4649 seems to be devoid of dust; no clear signal has been identified.

3.3.2. FIR Emission from Dust

Spitzer and Herschel provide data in the mid-IR and FIR with the Multiband Imaging Photometer for Spitzer (MIPS) and the Spectral and Photometric Imaging Receiver (SPIRE) instruments (Rieke et al. 2004; Griffin et al. 2010), observing at 24, 70, 160, 250, 350, and 500 μm. We used FIR dust maps and flux densities of the galactic sample listed in recent publications by Temi et al. (2007a, 2007b) and Amblard et al. (2014). The reader is referred to these publications to obtain details on the data reduction and the generation of calibrated images and derived flux densities.

[13] https://hla.stsci.edu/

[14] https://users.obs.carnegiescience.edu/peng/work/galfit/galfit.html

[15] https://photutils.readthedocs.io/en/stable

3.4. Hα+[N II] Emission from HST

We derived Hα + [N II] images for our sample galaxies, except for NGC 4406 (no HST Hα + [N II] image) using HST archival data. To remove the continuum, a wide-band image centered off the Hα + [N II] line was subtracted from the narrowband image centered on the Hα + [N II] line. The two filters were aligned, cropped to an identical size, and we used a linear regression to fit out the continuum emission from the narrowband filter (the regression can take into account cross-calibration error and the steepness of the galaxy SED, among other things).

The RANSAC Regressor algorithm from the Python library scikit-learn[16] was chosen to perform the regression in order to reject outliers in the data. The fit was also performed in a ring-shaped aperture to remove the main contribution from the Hα + [N II] line emission. The inner and outer radii of the ring were determined for each galaxy by verifying that little to no Hα + [N II] emission was present within the aperture (typical values for the inner and outer radii are about 5″ and 8″). The percentage of outliers for each regression remains below 15%, an acceptable level, and mostly comes from point sources in the image that were not subtracted away.

From the Hα + [N II] images, Hα + [N II] fluxes were calculated by summing up the pixel flux in a circular aperture centered on each galaxy. Assuming a uniform Gaussian noise, the statistical error on the flux was calculated by multiplying the median absolute deviation (scaled to the rms) of the background pixels with the square root of the number of pixels in the aperture. In addition we evaluated a systematic error, coming from our imperfect continuum subtraction, by propagating the estimated error on the regression coefficients (scaling factor with wide-band filter and background value). Due to residual point sources affecting the Hα + [N II] images, it is likely that we have underestimated this error to some degree.

Hα + [N II] emission, estimated from HST data, has been detected in NGC 4203, NGC 4261, and NGC 4374. The procedure described previously did not return any significant signal for the two other galaxies for which data were available (NGC 4552 and NGC 4649). We therefore decided not to include the resulting images. To compare the structure of Hα + [N II] with the structure of the dust in each galaxy, we overlaid a contour plot of the dust of each galaxy on the Hα + [N II] image. All images show extended Hα + [N II] emission and some level of correlation with the dust absorption.

3.5. Hα+[N II] Emission from SOAR and VMOS

M84 was observed with the Multi Unit Spectroscopic Explorer (MUSE) on 2019 February 6 and March 2, for four exposures of 600 s each. NGC 4261 was observed with MUSE on 2016 April 17, for six exposures of 870 s each. MUSE provides a spectroscopic data cube on a rectangular $1' \times 1'$ field, with a spectral coverage of 4800–9000 Å. The MUSE data were reduced using the v2.8.1 ESO MUSE pipeline. Further sky subtraction was done with the Zurich Atmosphere Purge (ZAP) software (Soto et al. 2016), using two sky observations (600 s each) taken along with the M84 exposures and empty sky positions for the NGC 4261 observations. We then fit the emission lines ([N II]λ6548, 6583, Hαλ6563, [S II] λ6716, 6731) using the KUBEVIZ code as in Fossati et al. (2016). Groups of lines were fitted simultaneously using a combination of 1D Gaussian functions with fixed relative velocities. The noise was measured from the "stat" data cube and renormalized on the line fluxes to take into account the correlated noise introduced by resampling and smoothing, as extensively described in Fossati et al. (2016).

[16] https://scikit-learn.org

Table 3
Summary of Chandra Observations

Galaxy	Obs. ID	Obs. Date	Detector	Exp. (ks)
NGC 4203	10535	2009-03-10	ACIS-S	42.1
NGC 4261	834	2000-05-06	ACIS-S	17.9
	9569	2008-02-12	ACIS-S	87.6
NGC 4374	803	2000-05-19	ACIS-S	25.9
NGC 4406	318	2000-04-07	ACIS-S	13.3
NGC 4552	2072	2001-04-22	ACIS-S	44.0
	13985	2012-04-22	ACIS-S	41.2
	14358	2012-08-10	ACIS-S	41.5
	14359	2012-04-23	ACIS-S	44.0
NGC 4636	323	2000-01-26	ACIS-S	48.8
NGC 4649	785	2000-04-20	ACIS-S	33.0
	8182	2007-01-30	ACIS-S	39.8
	8507	2007-02-01	ACIS-S	15.0
	12975	2011-08-08	ACIS-S	73.4
	12976	2011-02-24	ACIS-S	86.9
	14328	2011-08-12	ACIS-S	11.9

3.6. X-Ray Emission, Hot Gas, and Entropy

The reduction and analysis of the archival Chandra data follows the procedures described in Werner et al. (2012) and Lakhchaura et al. (2018). The data were cleaned to remove periods of anomalously high background. The observations are summarized in Table 3.

Background-subtracted images were created in six narrow energy bands, spanning 0.5–2.0 keV. These were flat fielded with respect to the median energy for each image and then co-added to produce the X-ray images shown in Figure 11.

In the first part of the spectral analysis, we measured the azimuthally averaged, deprojected radial distributions of densities, temperatures, and metallicities. We extracted spectra from concentric annuli with a signal-to-noise ratio of at least 18 (∼320 counts per region) and fitted them simultaneously in the 0.5–2 keV band using the PROJCT model implemented in the X-Ray Spectral Fitting Package (XSPEC; Arnaud 1996). The emission from each spherical shell was modeled with an absorbed Astrophysical Plasma Emission Code (APEC; Smith et al. 2001), thermal model (Foster et al. 2012), and all of the deprojected densities (n_e) and temperatures (kT) were determined simultaneously. We fitted two metallicity values for each galaxy, one for the shells outside the radius of ∼1 kpc and another for the central regions of the galaxies.

For galaxies with a sufficient number of X-ray photons, we produced 2D maps of projected thermodynamic quantities. The regions used for spectral mapping were determined using the contour binning algorithm (Sanders 2006), which groups neighboring pixels of similar surface brightness until a desired signal-to-noise threshold is met. For the line-rich spectra of the relatively cool galaxies in our sample, we adopted a signal-to-noise ratio of 18 (∼320 counts per region), which allowed us to achieve better than 5% accuracy in the temperature

measurements. The spectral fitting was performed using the SPEX[17] package (Kaastra et al. 1996). The spectrum for each region was fitted in the 0.5–2.0 keV band with a model consisting of an absorbed single-temperature plasma in collisional ionization equilibrium, with the temperature and emission measure as free parameters. The absorption column densities, $N_{\rm H}$, were fixed to the values determined by the Leiden/Argentine/Bonn radio survey of H I (Kalberla et al. 2005), and the metallicities were fixed to 0.5 solar (see Werner et al. 2012, for more details).

For all spectral fitting, we employ the extended C-statistics available in XSPEC and SPEX. All errors are quoted at the 68% confidence level for one interesting parameter ($\Delta C = 1$).

3.7. Radio Emission

The VLA radio observations in the A, B, C, and D configurations in the *L* band (at 1–2 GHz centered at 1.5 GHz) are reduced using NRAO CASA (McMullin et al. 2007) version 4.7.2 and 5.6.1. Two categories of the data are analyzed depending on the year of their observation: either the historical VLA data, which includes observations before an important VLA upgrade in 2011, or new Karl G. Jansky VLA data after this upgrade. The new observational data sets are available in the high-resolution VLA A configuration for sources NGC 4203 and NGC 4406 as well as in the more compact configurations C and D for NGC 4374, NGC 4552, NGC 4636, and NGC 4649. These new data were calibrated using the CASA pipeline version 1.3 and reduced by standard procedures as described in, e.g., Grossová et al. (2019). On the other hand, the historical VLA observations were manually calibrated using the NRAO pre-upgrade calibration methods.[18] A summary of observation details can be found in Table 4.

For most targets, the model by Perley & Butler (2013) for standard VLA calibrator 3C 286 was used to determine the flux scales, except for NGC 4552 and NGC 4649, both in A configuration, which were calibrated with 3C 48. The final total intensity images, for both new Karl G. Jansky VLA and historical VLA observations (Figures 15, 18), are created using the CASA MultiTerm MultiFrequency synthesis `clean` algorithm (Rau & Cornwell 2011) with the `briggs` (`robust = 0`) weighting scheme (Briggs 1995). When the dynamic range of the radio map (signal-to-noise ratio) reaches values of 100, the self-calibration method, consisting of three cycles of phase and one cycle of amplitude and phase calibration, is performed. The VLA data reduction details and the total flux densities are presented in Table 5.

4. Results

Table 6 summarizes the results of the SOFIA [C II] and CO observations. Three measured fluxes in the 158 μm emission line are reported, along with three 3σ upper limits. The listed CO fluxes are obtained either from the literature or calculated in this paper using data in the ALMA science archive. Since CO(1–0) fluxes were not available for all of the galaxies in the sample, we quoted the lowest-energy CO transition available.

NGC 4261 CO(2–1) flux was calculated using data in the ALMA science archive and recently published by Boizelle et al. (2021). Given the high angular resolution of the 12 m array data, some diffuse CO component might have been filtered out by the interferometer such as was the case for NGC 5044 observations, where the ALMA CO(2–1) flux was only 20% of the IRAM-30 m flux (David et al. 2014). The same caveat may apply for the CO(2–1) and CO(3–2) fluxes and upper limits of NGC 4374 and NGC 4649 as they were derived from ALMA data. The NGC 4374 flux was calculated by Boizelle et al. (2017) in the central 1″ radius of the galaxy (0.″3 resolution) although they noted that there is additional faint CO emission along the prominent dust lanes of this galaxy. The NGC 4649 CO(3–2) upper limit was calculated using the ALMA science archive. The CO upper limit fluxes are given for the ALMA beam size (generally subarcsecond), and they correspond to 3σ in a 500 km s^{-1} window. References to the CO fluxes from the literature are given in the table's caption.

Vila-Vilaró et al. (2003) found line ratios for elliptical galaxies on the scale of tens of arcseconds to be about 0.7 ± 0.2 (2.8 ± 0.9) for CO(2–1)/CO(1–0) in brightness temperature (flux) and 0.5 ± 0.3 (4.5 ± 3.0) for CO(3–2)/CO(1–0) in

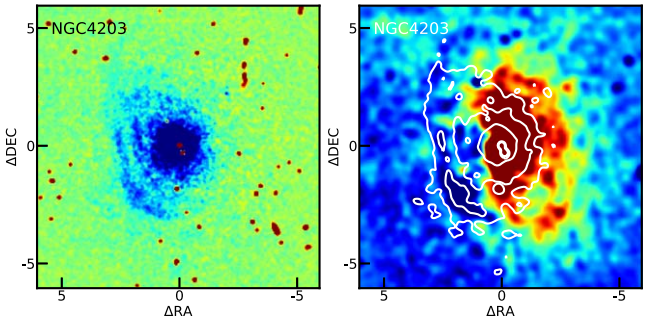

Figure 1. Left: NGC 4203 dust absorption map from HST. A stellar emission model obtained from either a "red" filter (F814W) or a functional form (ellipsoidal isophote from photutils or radial profile from GALFIT) is subtracted from the "blue" filter F555W observation. The dust absorption appears in blue in this color scale, zero emission is green, and the red area represents residual emission or emission bluer than the average stellar population in the galaxy. Right: HST Hα + [N ii] map. A stellar emission continuum is removed from a narrow filter. The dust absorption is overlaid with white contours.

Table 4
VLA Observational Details

Galaxy	Config/Band	Obs. ID	Obs. Date	TOS[a]
NGC 4203	A/L	15A-305	2015-Jul-03	3600
NGC 4261	A/L	AL0693	2007-Jun-08/09	2190
NGC 4261	C/L	AL0693	2008-May-24/25	2190
NGC 4374	A/L	AB0920	1999-Jul-18	2970
NGC 4374	B/L	BW0003	1994-Aug-04	1180
NGC 4374	C/L	14A-468	2014-Dec-24	5301
NGC 4406	A/L	15A-305	2015-Jul-02	3600
NGC 4552	A/L	AC301	1991-Aug-24	240
NGC 4552	C/L	16A-275	2016-Apr-04	2508
NGC 4636	A/L	AF0389	2002-Mar-12	12440
NGC 4636	C/L	17A-073	2017-May-25	5319
NGC 4649	A/L	AC0301	1991-Aug-24	260
NGC 4649[b]	B/L	AW0105	1984-Jan-24	4410
NGC 4649	D/L	17A-073	2017-Jun-01	5295

Notes.
[a] TOS: Time on source in seconds.
[b] Previously published by Dunn et al. (2010).

[17] www.sron.nl/spex
[18] https://casaguides.nrao.edu/index.php/Jupiter:_continuum_polarization_calibration.

Table 5
VLA Data Reduction Details of Sample Sources

Galaxy	Config/Band	Restoring Beam ($'' \times ''$)	Position Angle (deg)	rms Noise (Jy/beam)	$S_{1.5\ \mathrm{GHz}} \pm eS_{1-2\ \mathrm{GHz}}$ (Jy)	$P_{1-2\ \mathrm{GHz}} \pm eP_{1.5\ \mathrm{GHz}}$ (W/Hz)
NGC 4203	A/L	1.8×0.9	72.5	1.1×10^{-4}	$(7.8 \pm 0.3) \times 10^{-3}$	$(21.8 \pm 0.9) \times 10^{21}$
NGC 4261	A/L	1.4×1.3	−22.9	8.2×10^{-6}	$(1.72 \pm 0.07) \times 10^{-2}$	$(1.73 \pm 0.07) \times 10^{21}$
NGC 4261	C/L	18.8×13.5	51.8	1.4×10^{-3}	$(1.27 \pm 0.05) \times 10^{-1}$	$(1.28 \pm 0.05) \times 10^{22}$
NGC 4374	A/L	1.5×1.3	47.6	2.0×10^{-3}	$(4.78 \pm 0.23) \times 10^{-1}$	$(1.96 \pm 0.09) \times 10^{22}$
NGC 4374	B/L	4.6×4.4	−4.5	1.4×10^{-3}	$(4.18 \pm 0.17) \times 10^{0}$	$(1.71 \pm 0.07) \times 10^{23}$
NGC 4374	C/L	38.8×32.4	−45.2	5.8×10^{-3}	$(5.94 \pm 0.24) \times 10^{0}$	$(2.43 \pm 0.10) \times 10^{23}$
NGC 4406	A/L	1.1×1.0	−1.4	4.5×10^{-5}	$(2.77 \pm 0.53) \times 10^{-4}$	$(1.06 \pm 0.20) \times 10^{19}$
NGC 4552	A/L	1.4×1.1	13.6	2.7×10^{-4}	$(5.97 \pm 0.25) \times 10^{-2}$	$(1.83 \pm 0.08) \times 10^{21}$
NGC 4552	C/L	11.4×10.4	−26.5	2.6×10^{-4}	$(1.65 \pm 0.07) \times 10^{-1}$	$(5.05 \pm 0.21) \times 10^{21}$
NGC 4636	A/L	2.7×1.6	−74.7	4.4×10^{-6}	$(5.95 \pm 0.24) \times 10^{-2}$	$(1.81 \pm 0.07) \times 10^{21}$
NGC 4636	C/L	13.8×10.7	116.7	7.4×10^{-5}	$(6.91 \pm 0.28) \times 10^{-2}$	$(2.11 \pm 0.08) \times 10^{21}$
NGC 4649	A/L	1.4×1.3	−8.5	2.2×10^{-5}	$(1.44 \pm 0.06) \times 10^{-2}$	$(4.69 \pm 0.19) \times 10^{20}$
NGC 4649	D/L	11.5×9.1	−6.8	4.2×10^{-5}	$(2.83 \pm 0.11) \times 10^{-2}$	$(9.22 \pm 0.37) \times 10^{20}$

Note. Information derived from the radio total intensity maps produced with CASA. The table contains galaxy name, configuration and band, restoring beam size (resolution) and its position angle, rms noise, total flux density ($S_{1-2\ \mathrm{GHz}}$), and radio power ($P_{1-2\ \mathrm{GHz}}$) at 1–2 GHz.

Table 6
C II and CO Emitting Gas Properties

Galaxy NGC	$F_{\mathrm{C\ II\ (total)}}$ 10^{-13}erg cm^{-2} s^{-1}	$L_{\mathrm{C\ II\ (total)}}$ 10^{32} W	$v_{\mathrm{C\ II}}$ km s^{-1}	FWHM$_{\mathrm{C\ II}}$ km s^{-1}	F_{CO} 10^{-17}erg cm^{-2} s^{-1}	v_{CO} km s^{-1}	FWHM$_{\mathrm{CO}}$ km s^{-1}	[C II]/CO(1–0) 10^{3}	M_{mol} $10^{5}M_{\odot}$
4203	7.0 ± 1.4	19 ± 4	−61, 82	188, 120	3.7 ± 0.4[a]	−90	150	18.9 ± 4.3	230 ± 24
4261	2.5 ± 0.3	30 ± 4	172	672	3.8 ± 0.2[b]	−323, 247	342,318	18.4 ± 2.4	184 ± 9
4261 (2G)	2.4 ± 0.3	30 ± 4	−115, 319	310, 358	3.8 ± 0.2[b]	−323, 247	342, 318	17.5 ± 2.3	
4374	<0.5	<2.0			3.7 ± 0.5[c]	⋯	⋯	<4	61 ± 8
4406	0.9 ± 0.2	3.1 ± 0.7	−108	265	<3.5[d]			>2.6	<279
4552	<0.6	<1.8			<2.8[e]				<190
4649	<0.5	<1.8			<0.2[f]				<0.9
4636*	1.05 ± 0.04	2.7 ± 0.1	22	361	0.25 ± 0.01[g]	210	61	210 ± 43	2.6 ± 0.2

Notes. C II fluxes and luminosities obtained in this paper and in Werner et al. (2014) for NGC 4636*. When no emission was detected, a 3σ upper limit flux per beam in a central 500 km s^{-1} window is quoted. CO fluxes obtained from the literature or ALMA science archive, the CO upper limit fluxes, are given for ALMA beam size (generally subarcsecond); "upper limit" corresponds to 3σ in a 500 km s^{-1} window. The [C II]/CO(1–0) ratio was calculated using the Vila-Vilaró et al. (2003) observed line ratio.
[a] : CO(1–0) from Welch & Sage (2003),
[b] : CO(2–1) from this work using ALMA science archive,
[c] : CO(2–1) from Boizelle et al. (2017),
[d] : CO(1–0) from Wiklind et al. (1995),
[e] CO(1–0) from Combes et al. (2007),
[f] : CO(3–2) from this work using the ALMA science archive.
[g] : CO(2–1) from Temi et al. (2018).

brightness temperature (flux). These CO line ratios were used to compute the [C II]/CO(1–0) ratio column in Table 6; these ratios go from 2600 (lower limit) to about 19,000.

Several observations in the Galaxy show a wide range of [C II]/CO(1–0) ratios depending on the type of regions observed: photodissociation regions (PDRs), H II regions, CO-dark H_2 cloud, etc. (e.g., Wolfire et al. 1989; Pabst et al. 2017; Pineda et al. 2013; Langer et al. 2014). On theoretical grounds, several factors have been scrutinized that could influence the amplitude of the [C II] emission line intensity with respect to other molecular lines. For instance, Röllig et al. (2006) examined the influence of the metallicity on the [C II] emission in PDRs and found that the [C II]/CO(1–0) ratio decreases very rapidly with increased metallicity. They also calculated the influence of the far-UV (FUV) incident radiation, the clump mass, and the density and found that the [C II]-to-CO (2–1) ratio was increasing with FUV radiation, decreasing with clump mass, and decreasing with density. Varying all of these factors, they found that the [C II]/CO(1–0) ratio can vary from 10^3 to 10^6 in PDRs.

Given the large range of possible values, the many influencing factors and the uncertainty in our ratio measurements, it is hardly possible to draw strong conclusions from our galactic samples. The observed ratios are within the expected range (observationally and theoretically); NGC 4203 and NGC 4261 are observationally on the larger side for PDRs, but could be explained by a dominant contribution from the H II region or a CO-dark H_2 cloud or by a low-metallicity, high-FUV background, small clump mass or density.

In the central regions of brightest group galaxies, the line ratio Hα + [N ii]/[C ii] of these two co-spatial emissions usually spans a narrow range ∼1.5–2.5 with little radial variation for $r < 3$ kpc (Werner et al. 2014). This evidence suggests that the low-excitation C^+ ion could exist in the warm

Table 7
Galactic Sample FIR Flux Densities and Luminosities

Galaxy	$F_{70\mu m}$ (mJy)	$F_{160\mu m}$ (mJy)	$F_{250\mu m}$ (mJy)	$F_{350\mu m}$ (mJy)	$F_{500\mu m}$ (mJy)	Log(L_d) $L_\odot$	Log(M_d) $M_\odot$
NGC4203	933 ± 111	2701 ± 259	1153 ± 173	526 ± 84	191 ± 30	8.55 ± 0.10	5.79 ± 0.14
NGC4261	127 ± 11	375 ± 18	237 ± 36	309 ± 57	216 ± 33	8.52 ± 0.02	5.94 ± 0.05
NGC4374	67 ± 9	535 ± 61	239 ± 36	146 ± 22	119 ± 18	8.46 ± 0.11	6.21 ± 0.26
NGC4406	64 ± 8	90 ± 12	1 ± 27	7 ± 27	8 ± 20	5.04 ± 0.03	2.65 ± 0.42
NGC4552	96 ± 10	188 ± 16	2 ± 27	21 ± 4	18 ± 16	6.63 ± 0.03	3.50 ± 0.06
NGC4649	48 ± 7	0 ± 30	1 ± 31	0 ± 24	0 ± 19	8.32 ± 0.03	2.52 ± 0.03
NGC4636*	197 ± 12	185 ± 24	88 ± 13	33 ± 54	12 ± 15	7.74 ± 0.02	4.36 ± 0.07

Note. FIR flux densities and luminosities are from Spitzer and Herschel. Dust masses from SED modeling are from Amblard et al. (2014).

gas, and that a significant fraction of [C II] comes from the same gas that emits Hα, with the implication that the two gas phases have a common excitation mechanism (Werner et al. 2014; Canning et al. 2016).

Such a narrow range in the Hα + [N ii]/[C ii] ratio is not confirmed for the galaxies in our sample. Among the galaxies with detected [C II] emitting gas, the ratio extends from ∼0.1 in NGC 4203, to ∼12 in NGC 4406, with NGC 4261 and NGC 4636 showing ratios of ∼1.6 and ∼2.5, consistent with the findings of Werner et al. (2014). Moreover, the upper limits in the 157 μm line emission, reported for the remaining galaxies, imply Hα + [N ii]/[C ii] ratios of >7 (NGC 4374), >5.6 (NGC 4649), and >4.5 (NGC 4552) that are inconsistent with values found in group-center galaxies.

Table 7 presents the integrated flux density at all of the FIR bands along with the dust luminosity L_d and mass M_d. Dust mass and luminosity have been evaluated using the SED modeling software CIGALEMC (Serra et al. 2011) and MAGPHYS14 (Da Cunha et al. 2008), and by fitting some modified blackbody spectra to the FIR portion of our data ($\lambda > 60$ μm; see Amblard et al. 2014 for details). Both SED fitters are capable of modeling the galaxy SED from a UV to a millimeter wavelength and constraining the computed L_d and M_d by fitting the absorption in UV, optical, and the FIR emission consistently. Given the excellent sampling of the FIR SED for the entire galactic sample, the computed dust luminosity and mass are well constrained. It is worth noting that, although all of the galaxies have similar L_B, the dust luminosity ranges over more than two orders of magnitude. This is also reflected in the total dust content: on one extreme, NGC 4649 is consistent with a dust-free galaxy, while NGC 4261 accounts for $\sim 10^6 M_\odot$ of dust.

Below, we report the results from the new SOFIA and ALMA observations, combined with archival multiwavelength data, on an object-by-object basis. The outlined physical conditions of the ISM in each object will provide a baseline for the discussion and interpretation of the data. It should be noted that the units of ΔR.A. and Δdecl. in all of the maps throughout the manuscript are expressed in units of arcseconds.

4.1. NGC 4203

The ETG NGC 4203 has been classified as a fast rotator by Emsellem et al. (2011) and consistently shows a central disk of dusty gas. The HST dust map of the central ∼10″ shows a dusty central core with one or two arms in the south–north direction compatible with its face-on orientation. The central disk of dust extends ∼350 pc in diameter (Figure 1), and the filamentary structure is reminiscent of possible spiral arms.

The galaxy has a strong integrated FIR flux with a peak at 160 μm of ∼2.7 Jy (Amblard et al. 2014). Deep H I observations reveal a large gas reservoir (∼109 $M_\odot$), distributed in a disc with two distinct components (Yıldız et al. 2017). Both [C II] emission and CO(2–1) emitting gas have been detected at a systemic velocity of ∼−70 km s^{-1} and velocity dispersion of ∼150 km s^{-1}. The new SOFIA data reveal two distinct [C II] emission lines (Figure 2). The detections are compact and unresolved by the FIFI-LS instrument and localized within the central 2 kpc. The central Hα+[N II] gas emission, as revealed by the HST map (Figure 1), shows the ionized gas distributed in an ellipsoid of about 7″ major axis along the north–south direction with a larger emission in its western section. The lack of Hα+[N II] emission on the eastern side of the galaxy is correlated with arm-like features in the dust absorption estimate presented in Figure 1.

The X-ray observations of NGC 4203 are not very deep and suffer from a low number of detected counts when compared to the other galaxies (Figure 11). The X-ray morphology appears relatively spherically symmetric. However, the data, in combination with older observations using the Einstein X-ray Observatory (Fabbiano et al. 1992), show evidence of ram pressure stripping with a tail extending to the south. The nuclear radio emission observed at 1–2 GHz taken in several VLA configurations shows a weak point-source radio emission (Figure 18; top left).

4.2. NGC 4261

NGC 4261 is a giant elliptical E2 (from RC3) galaxy also known as the radio galaxy 3C270 (Birkinshaw & Davies 1985) and is the largest member of a group of 33 galaxies (Nolthenius 1993).

The HST dust absorption map of NGC 4261 (Figure 3) clearly shows a central disk of dust that extends ∼250 pc. Its size and location are well matched by the CO(2–1) data from ALMA (Figure 4). The interferometric data indicate a molecular gas rotation in the south–north direction of the molecular gas with a peak to peak amplitude of −350–250 km s^{-1}, which is similar to the dynamics of the ionized gas measured by the Hα emission. The peak to peak rotation amplitude is also similar to the [C II] measurement albeit a bit larger (amplitude of about 430 km s^{-1} for [C II] versus 570 km s^{-1} CO(2–1); Figure 5).

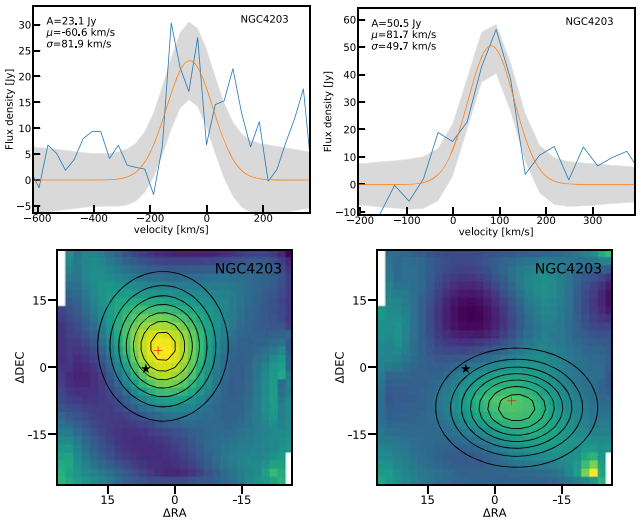

Figure 2. Top: NGC 4203 C II lines (blue solid lines) detected in SOFIA FIFI-LS. The orange solid lines represent a Gaussian fit to the line; the parameters of the Gaussian are indicated in top-left corner (A: amplitude, μ: velocity center, σ: velocity width), and the name of the galaxy is indicated in the top-right corner. The gray shaded areas indicate the noise level for each spectrum. Bottom: images at the wavelength of the line maximum emission for the two observed lines of NGC 4203; the black star indicates the position of the galaxy (NED coordinates), and the black contours represent a 2D Gaussian fit to the line source.

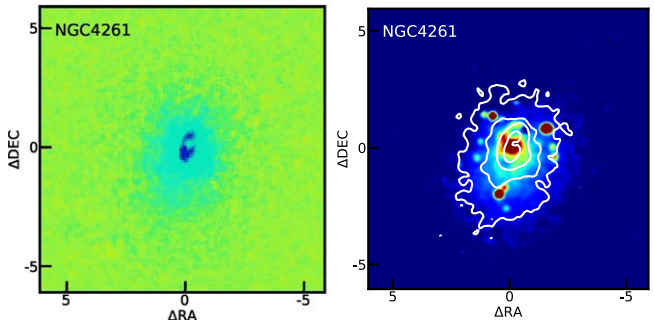

Figure 3. Left: HST dust absorption map of NGC 4261. The central disk of dust appears in dark blue in this color scale; zero emission is in green. Right: HST Hα + [N II] map. A stellar emission continuum is removed from a narrow filter. The dust absorption is overlaid with white contours.

The HST Hα+[N II] emission is distributed in a very compact, about 1″ major axis ring and a strong point-like central emission. The ring is elongated in the north–south direction similarly to the dust disk, visible in Figure 3. Both have a similar spatial extent, the dust absorption seems to be a bit more extended, but it could be due to a difference in the signal-to-noise ratio between the dust absorption and the Hα+[N II] emission estimates.

From the MUSE spectra (Figure 5), the Hα emitting gas exhibits a velocity range from -150 to 150 km s^{-1}. The rotation amplitude (300 km s^{-1}) of the ionized gas seems to be of the same order as the peak difference ($\sim$430 km s^{-1}) in the [C II] observations; the orientation can not be probed with [C II] due to the small extent of the gas distribution. The velocity dispersion is also of the same order (about 200 km s^{-1} FWHM). These similarities could hint at a common origin for these two lines.

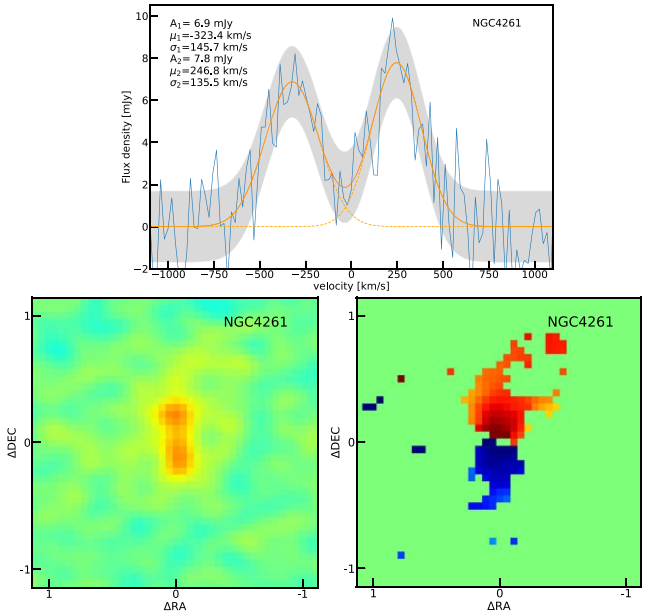

Figure 4. Top: spectrum of CO(2–1) emission lines (blue solid line) observed by ALMA (about 0.″3 angular resolution) with a 1″ radius aperture. The orange solid lines represent a Gaussian fit to the lines. Parameters of the Gaussians are indicated in the top left corner (A: amplitude, μ: velocity center, σ: velocity width), and the name of the galaxy in the top right corner. The gray shade area indicates the noise level. Lower left: intensity of the CO(2–1) emission integrated over the velocity. Lower right: velocity of the CO(2–1) emission line, the color scale goes from -350 to 350 km s^{-1} (blue to red).

The X-ray morphology appears relatively spherically symmetric (Figure 11). The radio emission observed at 1–2 GHz reveals powerful jets penetrating the atmosphere and depositing their energy at large radii (Figure 18; top middle). The disk of dust, as revealed by HST data, is aligned with its radio axis and is perpendicular to the stellar component of the galaxy (Jaffe et al. 1993).

4.3. NGC 4374

NGC 4374 (M84, also known as the FRI radio galaxy 3C272.1) is a giant elliptical E1 (from RC3) galaxy located in the core region of the Virgo cluster.

SOFIA observations have not detected cool [C II] emitting gas in NGC 4374; the flux upper limit is reported in Table 6. Although the [C II] line emission has not been detected, the galaxy exhibits extended, stratified dust seen in absorption in the nuclear region with a significant cold dust emission observed in the far-IR that accounts for a total dust mass of $1.6 \times 10^6 M_\odot$ (Figure 6). From HST data, NGC 4374 Hα+[N II] emission has a large number of features. A strong central emission is extended in the east–west direction by about 0.″5. Some antenna-like thin plumes point in the southern direction and extend about 1″ from the center of the galaxy. Some very large plumes extend more than 6″ in the eastern direction and about 3″ in the western direction. Multiple Hα + [N II] small substructures are visible within 2″ from the center of the galaxy. The largest scale features of the Hα+[N II] emission seem to correlate with the dust absorption as seen in Figure 6, although it appears that the dust is systematically located about 0.″5 northward of the Hα+[N II] emission. The velocity and velocity dispersion estimated with the MUSE spectra range

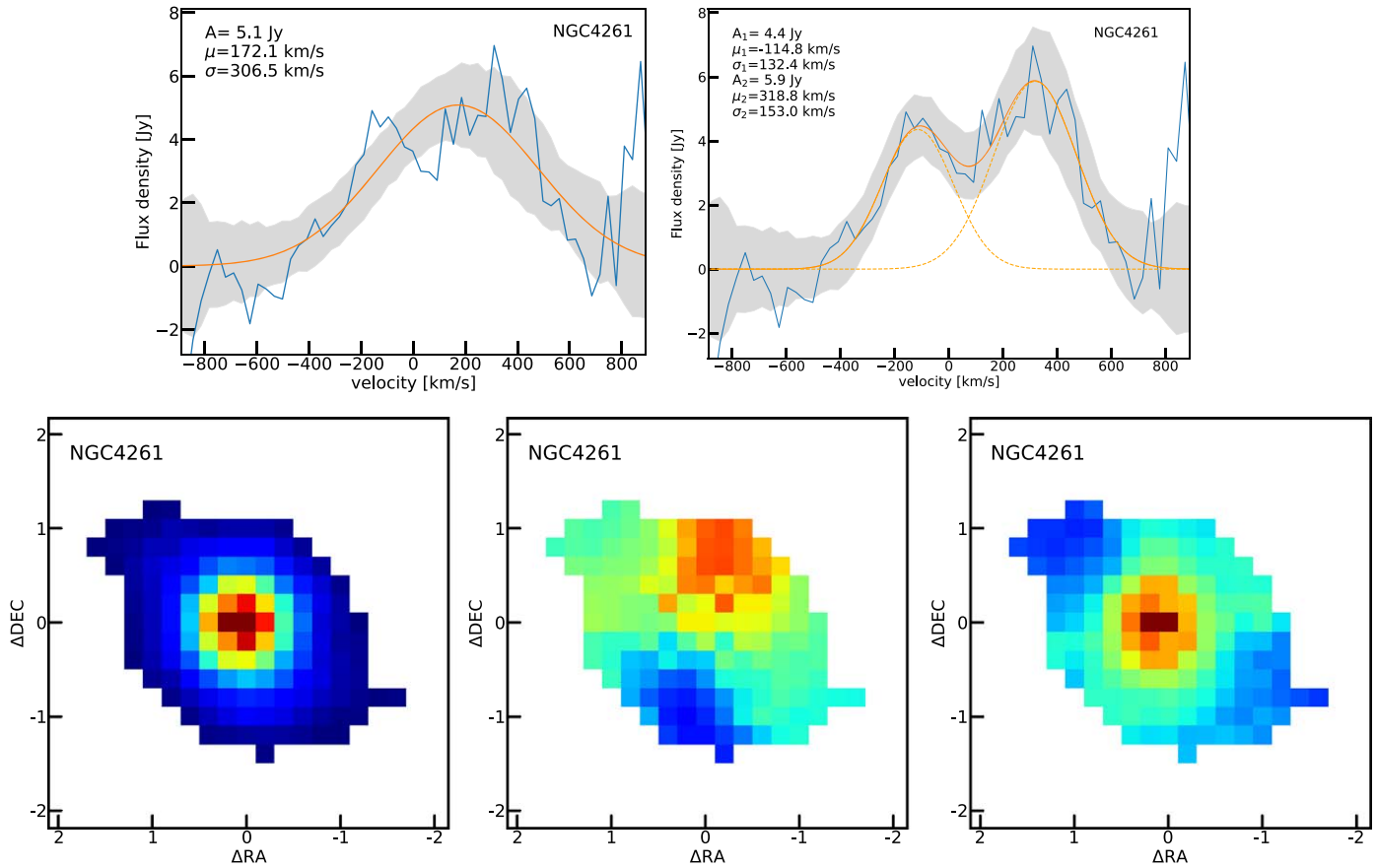

Figure 5. Top: C II lines (blue solid lines) detected with SOFIA FIFI-LS in NGC 4261. The orange solid lines represent a Gaussian fit to the line, the parameters of the Gaussian are indicated in top-left corner (A: amplitude, μ: velocity center, σ: velocity width), and the name of the galaxy in the top-right corner. The gray shaded areas indicate the noise level for each spectrum. The top-right panel shows an alternative fit for NGC 4261 with two Gaussian lines instead of one. Bottom: Hα emission (left), velocity (center), and velocity dispersion (right) estimated on MUSE spectra for NGC 4261. On the color scale, the velocity ranges from -150 to 150 km s^{-1}, the velocity dispersion ranges from 0 to 350 km s^{-1}. The Hα image is in units of 10^{-20} erg cm^{-2} s^{-1}. The rotation amplitude (300 km s^{-1}) of NGC 4261 ionized gas visible in the Hα seems to be of the same order as the peak difference (400 km s^{-1}) in the [C II] observations; the orientation can not be probed with [C II] due to the small extent of the gas distribution. The velocity dispersion is also of the same order (about 200 km s^{-1} FWHM). These similarities could hint a common origin for these two lines.

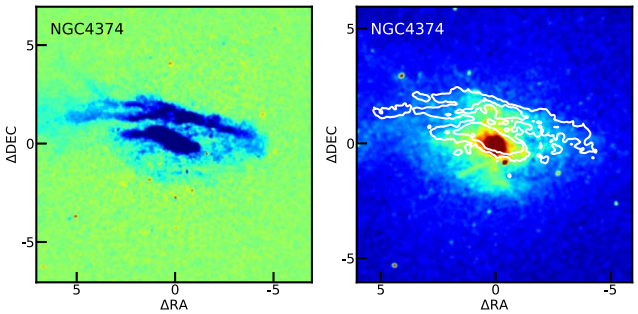

Figure 6. Left: HST dust absorption map of NGC 4374. The map appears in blue in this color scale, zero emission is green, and red areas represent residual emission or emission bluer than the average stellar population in the galaxy. Right: HST Hα + [N II] map. A stellar emission continuum is removed from a narrow filter. The dust absorption is overlaid with white contours.

from -250 to 250 km s^{-1} and from 0 to 250 km s^{-1}, respectively (Figure 7).

CO(2–1) in NGC 4374 has been detected in the central $\sim$1″ where the optical HST map shows a dusty disk with major axis misaligned by $\sim$90° with respect to the stellar one (Boizelle et al. 2017). NGC 4374 is classified as a slow rotator (Emsellem et al. 2011) with almost no line-of-sight stellar rotation. Both the cold molecular gas and ionized gas kinematics show disk rotation that appears to be misaligned with respect to the stellar axis by $\sim$90° (Walsh et al. 2010; Boizelle et al. 2017).

The X-ray morphology is strongly affected by AGN feedback. It shows extended "arms" of gas compressed by AGN-jet inflated radio lobes (see also Finoguenov & Jones 2001; Finoguenov et al. 2008; Figure 11). Radio emission observed at 1–2 GHz exhibits strong radio mode feedback within the inner parts of the galactic atmosphere (Figure 18; bottom left).

4.4. NGC 4406

NGC 4406 (M86) is a giant elliptical E3 (from RC3) galaxy located in the Virgo cluster. SOFIA has detected cool [C II] emitting gas located within the central 2 kpc. The detected gas is compact with a velocity dispersion of $\sim$115 km s^{-1} and is spatially unresolved by the FIFI-LS instrument (Figure 8).

Early IRAM single-dish observations in the CO(1–0) molecular gas have resulted in upper-limit flux with a corresponding upper limit in H_2 molecular mass of $M_{H_2} < 0.32 \times 10^8 M_\odot$ (Wiklind et al. 1995). The HST dust image shows some residual emission at its center and a plume along the radial direction extending $\sim$4″. Morphologically

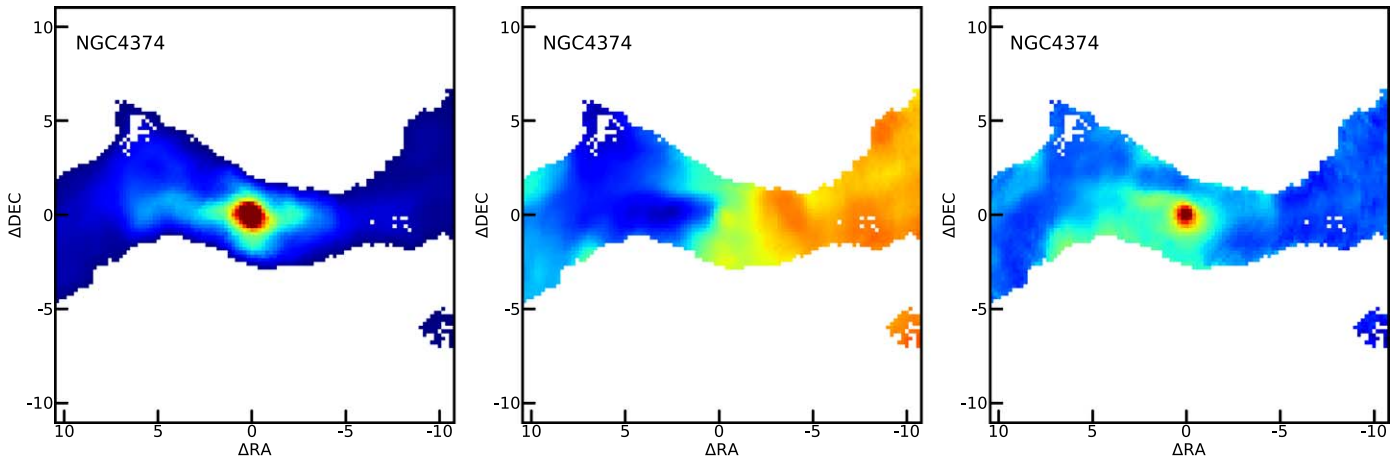

Figure 7. Hα emission (left), velocity (center), and velocity dispersion (right) estimated on MUSE spectra for NGC 4374. On the color scale, the velocity ranges from −250 to 250 km s^{-1}, the velocity dispersion range from 0 to 250 km s^{-1}. The Hα image is in units of 10^{-20} erg cm^{-2} s^{-1}.

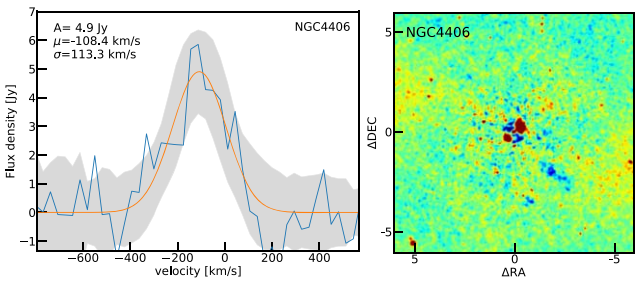

Figure 8. Left: C II lines (blue solid lines) detected with SOFIA FIFI-LS in NGC 4406. The orange solid line represents a Gaussian fit to the line, the parameters of the Gaussian are indicated in top-left corner (A: amplitude, μ: velocity center, and σ: velocity width), and the name of the galaxy is indicated in the top-right corner. The gray shaded area indicates the noise level in the spectrum. Right: HST dust absorption map. The dust absorption appears in blue in this color scale, zero emission is green, and the red areas represent residual emission or emission bluer than the average stellar population in the galaxy.

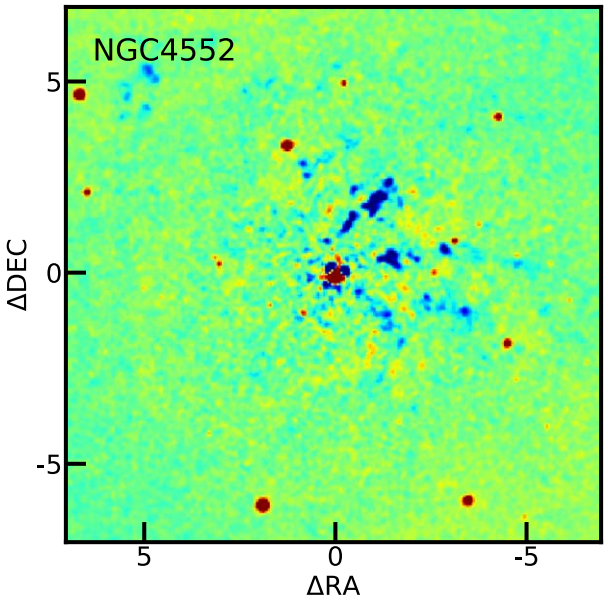

Figure 9. HST dust absorption map of NGC 4552. The dust absorption appears in blue in this color scale, zero emission is green, and the red areas represent residual emission or emission bluer than the average stellar population in the galaxy.

complex warm ionized gas has been detected through Hα emission (Kenney et al. 2008), linking NGC 4406 to the spiral galaxy NGC 4438, which lies 23′ (120 kpc) away. Using Herschel FIR detectors, Gomez et al. (2010) detected several dust clouds around NGC 4406 (total mass of 2–5 × 10^6 $M_\odot$), some of which (most massive) are colocated with the Hα emission, indicating the dust also comes from a collision with NGC 4438. X-ray observations of NGC 4406 do not display obvious indications of AGN feedback (Figure 11), but the galaxy is particularly strongly affected by ram pressure stripping, as it is supersonically falling into the Virgo cluster along a direction close to our line of sight (Randall et al. 2008). NGC 4406 shows at 1–2 GHz only point-like radio emission (Figure 18; top right).

4.5. NGC 4552

NGC 4552 (M89) is a giant elliptical E0 (from RC3) galaxy that is falling into the Virgo cluster (it is 350 kpc to the east of M87, in subcluster A). Cool [C II] emitting gas has not been detected in NGC 4552, and the upper limit is reported in Table 6.

The dust absorption map elaborated with HST data (see Figure 9) accounts for minimal dust seen in absorption in the nuclear region. There are hints of a few dust plumes along the radial direction extending out up to 4″/300 pc away from the galaxy center. Low level detection at far-IR wavelengths accounts for a mere 3500 $M_\odot$ of total dust estimated with the SED modeling software, CIGALEMC (Amblard et al. 2014), although larger dust masses have been reported in a recent paper by Boselli et al. (2022). Even if specific SED fitting codes could generate slightly different dust masses (similarly to Boselli et al. 2022, in this work we have used results, among others, derived from CIGALE SED code (see Section 4 and discussion in Amblard et al. 2014), we believe that most of the dust mass discrepancy is due to the evaluation of the diffuse and extended FIR emission that is given as input to the SED fitting process. There is indeed a significant difference between the two FIR sets of data (see Table 7, and Ciesla et al. 2012; Cortese et al. 2014). The discrepancy in the observed flux is puzzling, and can be ascribed to the procedures used to evaluate the radial extent of the diffuse low level emission.

CO has not been detected in NGC 4552: IRAM observations only provide a CO(1–0) flux upper limit (Table 6). Hα+[N II]

emission estimated from HST data did not return any significant signal. Early ground-based observations have reported Hα+[N II] emission in the central regions (Trinchieri & di Serego Alighieri 1991; Macchetto et al. 1996). More recent very deep narrowband Hα+[N II] imaging carried out with MegaCam at the Canada–France–Hawaii Telescope shows a diffuse and filamentary distribution of the ionized gas (Boselli et al. 2022). X-ray emission is detected at the center of the galaxy with a sharp edge 3.1 kpc to the north, a cool ($kT = 0.51^{+0.09}_{-0.06}$ keV) tail extending 10 kpc to the south of the galaxy, and two 3 kpc-long "horns" extending south on the sides of the north edge (Figure 11). The X-ray morphology is strongly affected by AGN feedback: the AGN shock-induced ring and the tail are interpreted as characteristic features of a supersonic ram pressure stripping of the gas, produced by the motion of NGC 4552 in the Virgo intracluster medium (ICM) and with an estimated infall velocity of 1680 km s^{-1} (Machacek et al. 2006a, 2006b). The galaxy has a radio source with jets extending to ~10 kpc along the north–south direction where the radio lobes coincide with cavities in the X-ray images (Shurkin et al. 2008).

4.6. NGC 4636

As mentioned before, NGC 4636 is not a member of the original SOFIA [C II] galactic sample. It is part of the galactic sample observed in the [C II] line by the Herschel observatory (Werner et al. 2014), and here it serves as a term of comparison for the interpretation and understanding of feedback processes acting on the galaxies under investigation. Cold gas in the group-centered elliptical galaxy NGC 4636 has been reported in recent publications (Werner et al. 2014; Temi et al. 2018). A map of the integrated [C II] line flux obtained with Herschel PACS shows extended emission, presumably in filamentary structures, in the central ~3 kpc with a velocity dispersion of ~350 km s^{-1} (Werner et al. 2014). The extended [C II] line emission is co-spatial with near-infrared H_2 emission and filamentary structures in the Hα + [N II] nebula. CO(2–1) molecular gas is detected in the form of off-center orbiting clouds distributed in the center of the galaxy. The new ALMA CO(3–2) data confirm the presence of a compact molecular cloud a few arcseconds off the center. The associated total molecular mass is estimated to be $2.6 \times 10^5 M_\odot$. Small, chaotically arranged dusty fragments and filamentary structures are visible in HST dust absorption maps (Temi et al. 2018). The Hα + [N II] emission is extended, but remains relatively compact concentrated in the innermost $r \leqslant 1.5$ kpc of the galaxy with the peak centered in the optical galactic nucleus. Filamentary structures and bright compact knots are apparent in the central few kiloparsecs of the galaxy. NGC 4636 exhibits strong radio mode feedback within the inner parts of the atmosphere. Radio observations show AGN jets with energy deposited just outside a central, compact, X-ray bright, gaseous core of NGC 4636 (Figure 18; bottom right). The X-ray gas morphology appears affected by AGN feedback, showing "arms" of gas compressed by AGN-jet inflated radio lobes (see also Finoguenov et al. 2008; Baldi et al. 2009).

4.7. NGC 4649

NGC 4649 (M60) is a giant elliptical E2 (from RC3) galaxy at the eastern edge of the Virgo cluster and has a neighboring

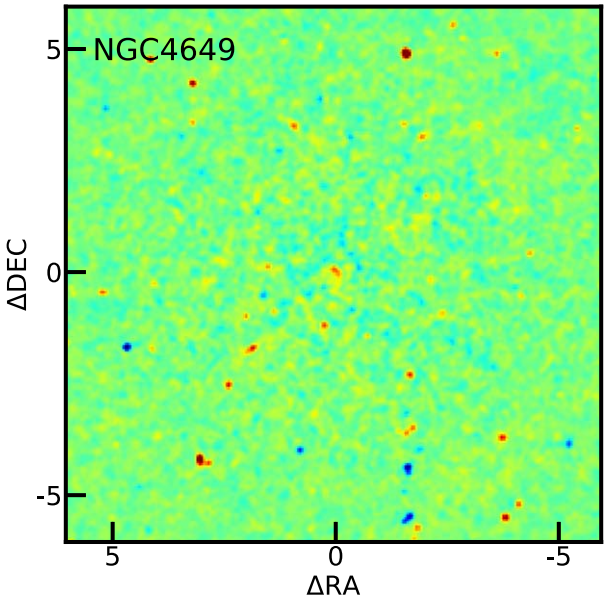

Figure 10. HST dust absorption map of NGC 4649. There is no evidence of dust in absorption in the central ~1.2 kpc.

spiral Sc galaxy NGC 4647 ~2.′5 away. NGC 4649 appears to be a truly cold-gas-free galaxy: (i) SOFIA FIFI-LS observations, although not very deep, did not detect [C II] emitting gas, and (ii) the dust absorption map elaborated with HST (see Figure 10) shows no evidence of dust in the central kiloparsec. Also, far-IR cold dust emission has not been detected in this galaxy—early ISO null observations (Temi et al. 2004) have been confirmed at 160 and 250 μm with an estimated total amount of dust of the order of 300 $M_\odot$, and finally, (iii) recent ALMA observations do not reveal any CO molecular gas in the central ~30″.

Trinchieri & di Serego Alighieri (1991) reported Hα + [N II] emission in the central region of NGC 4649, but more recent measurements with Astrophysical Observatory of the Smithsonian Institution/SOAR do not confirm detection. The X-ray gas morphology in NGC 4649 (Figure 11) appears spherically symmetric and apparently undisturbed by AGN energy release. In relation to the reported faint nuclear radio source, small disturbances in the X-ray-emitting gas (Shurkin et al. 2008; Dunn et al. 2010; Humphrey et al. 2013) have been reported on <3 kpc scales, corresponding to ~40″. Shurkin et al. (2008) showed X-ray cavities at the location of radio lobes (northeast and southwest) that extend ~20″. Using deep X-ray images, Humphrey et al. (2008) and Paggi et al. (2017) did not find convincing evidence of any morphological disturbances, reporting a relaxed and symmetric X-ray morphology at scales from 3 to 12 kpc. On large scales (>160″, 12 kpc), Wood et al. (2017) showed some evidence of ram pressure stripping (edge in the surface brightness and wing-like structures) due to the motion of the galaxy in Virgo ICM. Lanz et al. (2013) and D'Abrusco et al. (2014) suggested tidal interaction between NGC 4649 and NGC 4647 based on the shape of their SEDs and the spatial distribution of low-mass X-ray binaries. VLA radio data at 1–2 GHz show a weak radio source with small-scale jets extending to ~6 kpc along the north–south direction where the radio lobes coincide with cavities in the X-ray.

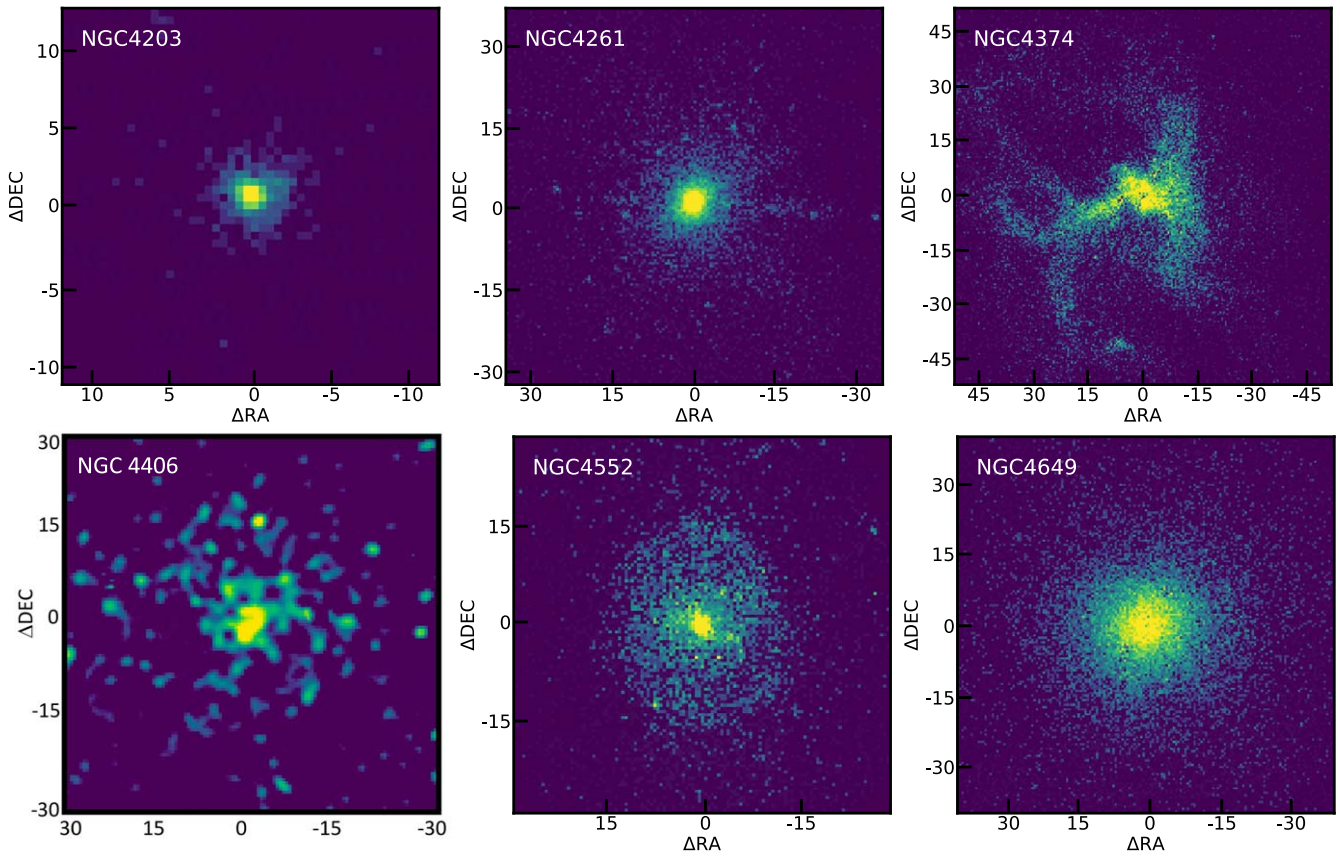

Figure 11. X-ray flux images in the 0.5–2 keV band of the galactic sample.

5. Discussion

Given the large multiwavelength data set available for the galactic sample presented here, we wish to discuss in detail the content, kinematics, and spatial distribution of the observed multiphase gas. Although small, our galactic sample shows a remarkable diversity of systems with a substantial range of cold/warm gas content, distribution, and kinematics. Thus, in combination with the thermodynamical properties of the hot gas, and the analysis of the radio properties in terms of morphology and energy power deposition, we wish to establish a path for the evolution of the gas in these galaxies that reflects their current physical condition.

SOFIA FIFI-LS observations reveal [C II] line emission in three (NGC 4203, NGC 4261, and NGC 4406) out of six observed galaxies. Multiwavelength data for NGC 4649, one of the three galaxies undetected in [C II], do not show the presence of any other cool or cold gas phases or significant amounts of dust. NGC 4552 eluded [C II] detection and shows inconsistent data regarding its cold gas content: in addition to [C II], it has not been detected in CO and shows a large discrepancy in the amount of dust accounted for via SED fitting procedures. On the other hand, NGC 4374 (M84) displays filamentary Hα+[N II] emission, dust, and molecular gas. The nondetection of [C II] emission in this system is therefore all the more puzzling. In our galaxies (except for NGC 4636), the distribution of the detected cool gas phases is centrally concentrated and fairly compact. The molecular gas spans a range of masses from $6.1 \times 10^6\ M_\odot$ in NGC 4374 to $2.3 \times 10^7\ M_\odot$ in NGC 4203. Both in the cool-gas-rich and cool-gas-poor galaxies (except M86, which might be an outlier due to its supersonic merger through the Virgo cluster), the X-ray emitting gas has relatively steep entropy profiles, and the radio jets are on, depositing their energy in the hot atmospheres of the galaxies.

5.1. Origin of the Cold Gas

The origin of the cold gas in massive ellipticals is still a matter of debate. While minor mergers may be responsible for a significant fraction of the cold gas mass in low-to-intermediate-mass ETGs (e.g., Davis et al. 2011), internal sources of neutral/molecular material, like hot gas cooling and stellar mass loss, are likely dominating the cold gas budget in massive ellipticals (Davis et al. 2011; David et al. 2014; Lagos et al. 2014; Werner et al. 2014; Valentini & Brighenti 2015; Sheen et al. 2016; Gaspari et al. 2017, 2018; Babyk et al. 2019). Moreover, the distribution and dynamics of the warm ($T \sim 10^4$ K) ionized gas can provide additional clues to the origin of the multiphase gas. Table 8 gives a qualitative summary of the multiphase gas status in the investigated galaxies.

Figure 13 shows the deprojected entropy profiles of the hot X-ray emitting gas of the individual galaxies along with the cooling time $t_{\rm cool}$ and the $t_{\rm cool}/t_{\rm ff}$ ratio, where $t_{\rm ff}$ is the freefall time. The method used to derive the profiles is presented in detail in Lakhchaura et al. (2018). The colored solid lines refer to the radial profiles of our galactic sample. Black lines identify galaxies from the sample of group-centered ellipticals studied by Werner et al. (2014). Their investigation reveals a clear separation in the radial profiles of thermodynamic properties of the hot gas between the galaxies that exhibit extended filamentary structures in the cool gas phase and the galaxies without cool gas. Such a distinction is apparent in Figure 13

Table 8
Summary of the Multiphase Gas Properties

Galaxy	Cold Gas Reservoir	Hα + [N II] Gas Morphology	X-Ray Gas Morphology	Radio Morphology	P_{jet} [a] (10^{42}erg s^{-1})	P_e [b] (erg cm^3)	K[c] (keV cm^2)
NGC 4203	Yes, detected in [C II], CO, Dust	Central, compact	Affected by ram pressure stripping	Faint point-like radio source	⋯	4.7 ± 1.6	10 ± 2
NGC 4261	Yes, detected in [C II], CO, Dust	Central, compact disk	Relaxed; spherically symmetric	Large power, jets penetrating the atmosphere and depositing energy at large radii	21.5 ± 4.3	27.0 ± 0.2	7.5 ± 0.3
NGC 4374	Yes, detected in CO, Dust	Extended	AGN disturbed, arms of compressed gas	Strong radio mode feedback within the inner parts of the atmosphere	15.3 ± 4.6	24.5 ± 0.2	8.5 ± 0.4
NGC 4406	Yes		Affected by ram pressure stripping	Faint point-like radio source	⋯	2.0 ± 0.1	15 ± 1
NGC 4552	No[d]		AGN disturbed, ring and tail	Strong radio mode feedback within the inner parts of the atmosphere	1.6 ± 0.4	21.3 ± 0.5	7.3 ± 0.3
NGC 4649	No		Relaxed; spherically symmetric	Small lobes in the central region	1.3 ± 0.4	72 ± 10	8.5 ± 0.1
NGC 4636	Yes, detected in [C II], CO, Dust	Extended; Filamentary	AGN disturbed, arms of compressed gas	Strong radio mode feedback within the inner parts of the atmosphere	0.30 ± 0.08	18.3 ± 0.4	5.6 ± 0.2

Notes.
[a] The mechanical power output of the AGN (including both jets) is taken from from Allen et al. (2006), Shurkin et al. (2008), and Kolokythas et al. (2018);
[b] Central pressure at 0.5 kpc;
[c] Entropy at 2 kpc;
[d] See discussion in Section 5.1.2.

where the solid black lines refer to galaxies with extended cool gas, and the dashed black lines identify galaxies almost free of cool gas. NGC 4636 (green solid line), the galaxy with extended and filamentary cool gas that the two samples have in common, traces the upper envelope of the solid black lines. The dichotomy in the entropy profiles in Werner et al. (2014) supports the scenario in which the cold gas originates from the cooling of the hot gas phase: the condition of low core entropy in such cold gas-rich galaxies promotes nonlinear density perturbations able to trigger very frequent and extended top-down cooling (Gaspari et al. 2012, 2013; Sharma et al. 2012; Werner et al. 2014; Brighenti et al. 2015; Valentini & Brighenti 2015; Voit et al. 2015; Li et al. 2015). On the other hand, our sample is likely covering the second phase of the internal self-regulation cycle, in which the halo tends to be overheated and in the more quiescent rotating stage. Indeed, with the exception of NGC 4636, the other galaxies in our sample with CO emission (Table 6) show that molecular gas is in the form of compact clouds or, as in NGC 4261 and NGC 4374, in a compact rotating disk. Similarly the [C II] emitting gas is observed in compact regions near the center, with the warm Hα + [N II] gas being more extended. This differs from several cold gas-rich galaxies studied by Werner et al. (2014). Figure 13 further shows that their entropy and cooling time radial profiles tend to overlap with the profiles identified by galaxies with low or no cool gas in the Werner et al. (2014) sample, albeit the scatter is large, above 0.5 dex. Our sample does not show a strong separation in entropy or cooling time profiles among galaxies with or without nuclear cool gas, suggesting that such galaxies are in a different mode of the condensation cycle, rather than in the more extended precipitation stage. We will discuss in Section 5.1.2 other key diagnostics of the condensation scenario; in particular, the C-ratio $\equiv t_{\rm cool}/t_{\rm eddy}$ (unlike the $t_{\rm cool}/t_{\rm ff}$) is better suited to unveil the different condensation regimes between central and noncentral galaxies, with the latter expected to develop a nuclear rain rather than extended filaments. The amount of molecular gas mass in the two parent samples shows another difference with Werner's sample. Table 6 reports the molecular gas mass based on the conversion from the CO flux. The molecular mass is computed by using (Bolatto et al. 2013)

$$M_{\rm mol} = 1.05 \times 10^4 \left(\frac{X_{\rm CO}}{2 \times 10^{20}}\right) \frac{S_{\rm CO}\Delta\nu\ D_L^2}{(1+z)}\ M_\odot, \qquad (1)$$

where $S_{\rm CO}\Delta\nu$ is the integrated line flux density in jansky kilometers per second in the ground rotational transition $J = 1 \rightarrow 0$, D_L is the luminosity distance to the source in megaparsecs, and z is the redshift. We use the *reference* conversion factor $X_{\rm CO} = 2 \times 10^{20}$ cm^{-2} (K km s^{-1})$^{-1}$ to evaluate the molecular gas mass in each galaxy. When detected, the mass of the cool gas phase in our galactic sample is often larger than the total mass of molecular gas detected in the central group galaxies that exhibit diffuse and filamentary cool gas extending to several kiloparsecs (Werner et al. 2014; Temi et al. 2018). For instance, the group-centered elliptical galaxies, NGC 5846, NGC 4636, and NGC 5044, have extended and filamentary Hα emission that is well matched by the gas emitting the [C II] line. They have molecular gas in the form of off-center orbiting clouds with associated total molecular mass from $2.6 \times 10^5 M_\odot$ in NGC 4636 to $6.1 \times 10^7 M_\odot$ in NGC 5044 over a region extending over a few kiloparsecs (David et al. 2014; Temi et al. 2018). In contrast, the three sample galaxies NGC 4261, NGC 4203, and NGC4374 have molecular gas masses of $1.8 \times 10^7 M_\odot$ within

$\sim$200–300 pc, $2.3 \times 10^7 M_\odot$ within $\sim$300 pc, and $6.1 \times 10^6 M_\odot$ within $\sim$200pc (Boizelle et al. 2017), respectively.

It is worth noting that, even considering the large range in molecular gas mass of the galaxies discussed here, they all show very low values of H_2 mass when compared to a large survey of ETGs. Figure 14 shows the molecular gas mass to stellar luminosity ratio plotted against Ks-band luminosity. The blue symbols identify galaxies in our sample and the parent sample of Werner et al. (2014) of the objects that have been detected in CO with ALMA (Temi et al. 2018). It is known that ALMA observations of CO emitting gas in these galaxies are not accounting for the large-scale diffuse CO emission, if present. In group-centered galaxies like NGC 5044 and NGC 5846, the ALMA integrated flux density is only $\sim$20% of that in the IRAM 30 m data, due to the presence of diffuse emission that is resolved out in the ALMA data (e.g., David et al. 2014; Temi et al. 2018). Nonetheless, when compared to large ETG surveys, their detected CO fluxes account for much lower H_2 masses. ALMA deeper observations allow us to explore for the first time the parameter space occupied by the galaxies investigated here.

Multiple sources may be at play to account for the cold gas present in our galactic sample. Driven by the results from the extensive data available, in the next sections, we examine and evaluate possible scenarios for the origin of the cold gas in our sample.

5.1.1. External Origin of the Cold Gas

The reported results show some similarity with the findings of a study of a sample of low-excitation radio galaxies (LERGs; i.e., giant elliptical galaxies) by Ruffa et al. (2019a, 2019b). The analysis of the molecular gas component in a volume-limited sample of LERGS shows that rotating (sub)kiloparsec molecular disks are common in LERGs. The bulk of the gas in the disks appears to be in ordered rotation and is co-spatial with dust lanes and disks of dust. For several targets, they also find evidence in support of a possible external origin of the gas, indicating that the environment in which the galaxies reside has a significant impact on the generation of their cool gas. On the other hand, other observed samples of massive galaxies with rotating gas/disks show evidence of internal condensation (e.g., Juráňová et al. 2019, 2020). In our sample, rotating (sub) kiloparsec gas disks, revealed in CO emitting gas and dust extinction maps, are observed in three out of five systems that have a cold gas reservoir (see Section 4).

It is very unlikely that group-centered elliptical galaxies, like the galaxies probed by Werner et al. (2014), David et al. (2014), and Temi et al. (2018), have acquired their cold gas via recent mergers with dust-rich galaxies. In most cases, this is corroborated by several lines of evidence, like the lack of any optical evidence for recent mergers, the mean stellar ages that are too old to be consistent with a recent merger, or the FIR emission that does not correlate with H_β stellar ages (Temi et al. 2005). In contrast, galaxies in our sample live in more diverse environments characterized by lower galaxy density, small groups, and pairs such that it is conceivable that they may have acquired at least part of their gas externally via galaxy–galaxy interactions (e.g., Sabater et al. 2013). Indeed lines of support include: (*i*) recent observations of Hα emission in NGC 4406 (Kenney et al. 2008), some of which is colocated in the region of its X-ray plume, suggest a collision with NGC 4438 as its origin; (*ii*) NGC 4261 has a well-defined disk of dust, 240 pc in diameter, that is aligned with its radio axis and perpendicular to the stellar component of the galaxy; (*iii*) in NGC 4374, the dust lane major axis is strongly misaligned with the major axis of the stars, and the kinematics of molecular gas is inconsistent with a stellar mass-loss origin; and (*iv*) the giant elliptical NGC 4552 that is falling into the Virgo cluster has central X-ray emission features (Machacek et al. 2006a) characteristic of a supersonic ram pressure stripping of the gas, produced by its motion in the Virgo ICM. Overall, albeit suggestive, these remain qualitative features that require further testing with future targeted and deeper observations.

5.1.2. Top-down Condensation

Considering that our sample of galaxies harbor a supermassive black hole (SMBH) at the center, it is expected that AGN feeding and feedback still plays an important role in shaping and regulating the cool gas content in these systems.

In the AGN self-regulation cycle, the feedback and accretion onto the SMBH are effectively linked over nine orders of magnitude (see Gaspari et al. 2020 for a recent review). Feeding via cold cloud condensation (known as chaotic cold accretion, CCA; Gaspari et al. 2013) triggers kinetic feedback in the form of jets and outflows, which can re-heat the hot halo and later stimulate thermal instability via turbulence (Yang et al. 2019; Wittor & Gaspari 2020), further inducing filamentary condensation and accretion. This creates a self-regulated duty cycle, which alternates between periods of more intense CCA rain and more quiescent overheated periods.

In the following section, we compare the multiphase gas observations for our galactic sample with key features as predicted by such AGN feeding and feedback scenarios at different stages of the cycle, to test consistency with the top-down condensation.

Cool gas-free galaxies—NGC 4649 shows no evidence of cool gas. The galaxy eluded detection in CO and [C II] lines and in dust emission via deep Spitzer observations. Warm Hα + [N II] emitting gas has not been securely detected either. As mentioned in Section 5, the cold gas content in NGC 4552 shows some inconsistency. On one hand, the nondetections in the [C II] emitting gas as well as in the CO line indicate that the cold gas reservoir, if present, it is not large. On the other hand, because of the nondetection in the CO line emission, Boselli et al. (2022) estimated a mass of molecular gas log $M_{H_2} = 8.63$ $M_\odot$ derived from the total dust mass and a gas-to-dust ratio of 80, rather than using the canonical conversion from Equation (1).We regard NGC 4552 as a system with low cold gas content; however, given the inconsistent data available on the derived molecular gas mass, a note of caution is advised. Figure 15 shows VLA radio data at 1–2 GHz. Both galaxies host a weak radio source with small-scale jets extending to $\sim$10 kpc in NGC 4552 and $\sim$6 kpc in NGC 4649. The symmetric X-ray gas morphology and the lack of a cold gas reservoir in conjunction with a very weak AGN jet may be indicative of a specific stage in the AGN self-regulation cycle. This is indeed the AGN starvation phase caused by a lack of the cold gas fuel: cool gas, previously condensed from the hot phase via cooling instabilities, is heated and eventually destroyed past the intense AGN feedback episode where large kinetic energy is released to the surrounding medium. The injected energy drastically reduces the cold gas fuel in the nuclear region, which, in turn, reduces the SMBH accretion

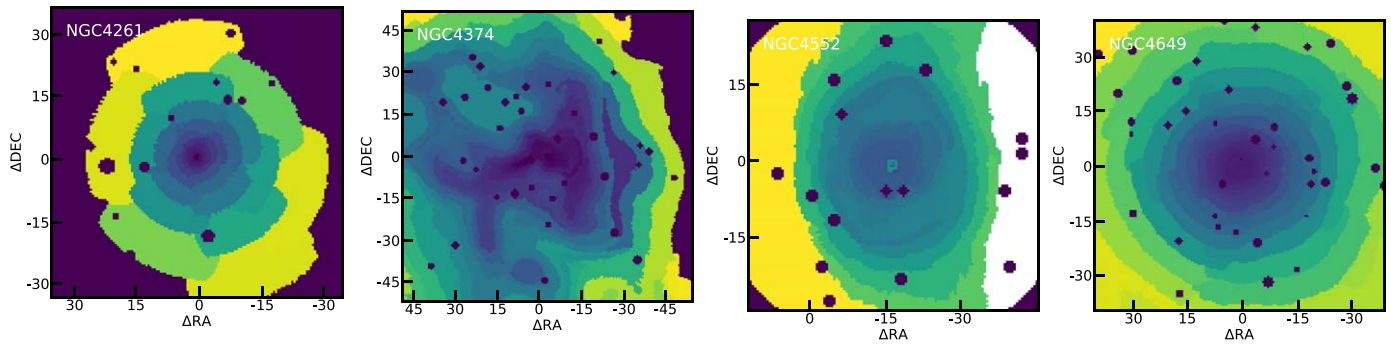

Figure 12. X-ray entropy of NGC 4261, 4374, 4552, and 4649.

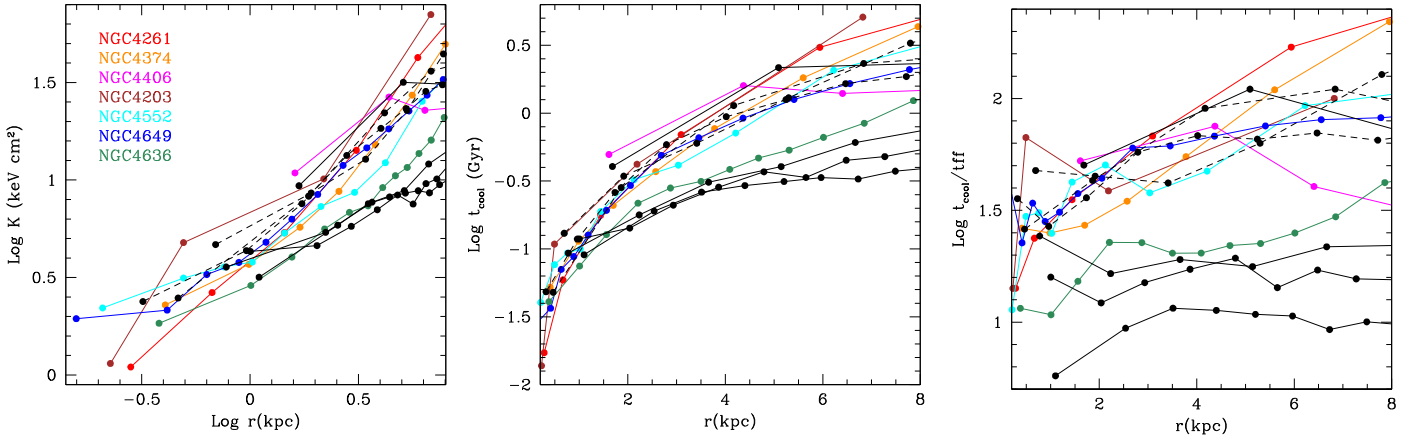

Figure 13. Deprojected entropy K, $t_{\rm cool}$, and $t_{\rm cool}/t_{\rm ff}$ ratio radial profiles. The colored solid lines refer to galaxies in our sample. Black lines identify galaxies with (solid) and without (dashed) extended cool gas in a parent sample studied by Werner et al. (2014). The solid green line refers to NGC 4636, the galaxy with extended and filamentary cool gas that is in common between the two samples.

rate and eventually brings the jet activity to a halt (e.g., Gaspari et al. 2012).

NGC 4649 is approaching this phase where the AGN feedback energy release is drastically decreasing due to the lack of a cold gas reservoir. This is also consistent with the current thermodynamic properties of the hot gas. The central gas pressure is the highest among all of the galaxies in the sample (see Table 8). In addition, the hot gas pressure and entropy maps are regular, smooth, and symmetric when compared with the thermodynamic maps of the cool gas galaxies (Figure 12). The regular and thermally stable hot atmosphere extends to large radii, supporting the hypothesis that the energy injected by the AGN has cleared most of the cool gas from the core and has propagated farther out, with the result of increasing the hot gas entropy. NGC 4552, the other galaxy with no or a very small cool gas reservoir, displays a hot atmosphere with similar thermodynamic properties, but the X-ray gas morphology shows signs of imprints left by recent AGN energy release (Machacek et al. 2006b).

Overall, our elliptical galaxies devoid of cool gas support the hypothesis that we are witnessing them during the more quiescent, overheated phase of the AGN feeding and feedback cycling, with both highly suppressed CCA rain and top-down condensation.

Galaxies with a cool gas reservoir—The spatial distribution and kinematics of CO and [C II] emitting gas in NGC 4203, NGC 4261, and NGC 4636 are both in excellent agreement. The velocity structure measured in NGC 4203 and NGC 4261 indicates that the cold gas in these systems is distributed in rotating structures with well matched velocity and velocity dispersion in the two gas phases. Central dust absorption as revealed by HST data exhibits a similar spatial distribution. Except for the lack of detected [C II] emitting gas, NGC 4374 reveals cold gas presence via the CO (Boizelle et al. 2017) and dust emission. The warm gas probed by the Hα+[N II] line emission roughly correlates with the spatial distribution of the colder component.

The diversity of the galaxies in terms of environment in which they reside in and their dynamical status may induce the scatter seen in their thermodynamic profiles (Figure 13), while still being consistent with variations driven by the AGN self-regulation cycle. The presence of cool gas in the fast rotator NGC 4203 could be enhanced by rotation. Indeed, cool gas can form and slowly accumulate in the central region because of the reduced feeding rate onto the SMBH due to the centrifugal barrier (Brighenti & Mathews 1996; Gaspari et al. 2015). For example, Juráňová et al. (2019, 2020) found favorable conditions for the development of multiphase gas condensations (with C-ratio $\sim$1) in a sample of six massive ETGs with rotating gas, even with relatively large $t_{\rm cool}/t_{\rm ff}$ ratios.

Figure 16 shows one of the key CCA diagnostics, i.e., the line broadening versus the line shift in logarithmic space (Gaspari et al. 2018). This kinematical plot ("k-plot") is key to dissecting the different cooling elements, in particular comparing the relative importance of turbulence (ordinate) versus bulk motions (abscissa). The blue points depict the detected cool gas in our galaxies via [C II] and CO, whenever available (see Table 6). The green contours are the 1σ–3σ confidence-level

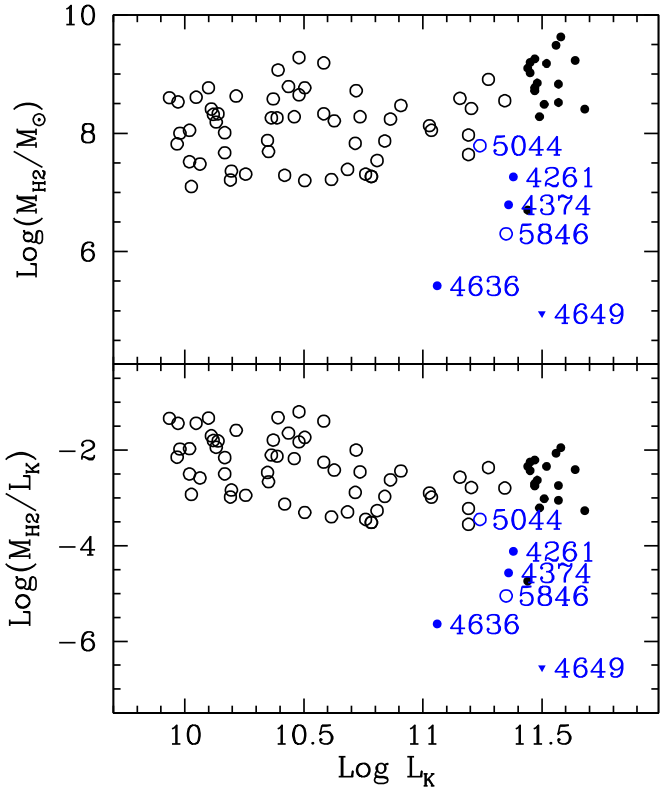

Figure 14. Molecular gas mass (top panel)and molecular gas mass to stellar luminosity ratio (bottom panel) plotted against Ks-band luminosity. Black circles refer to MASSIVE (solid circles) and ATLAS3D (open circle) CO detected survey galaxies from Davis et al. (2019) and Young et al. (2011). Blue circles represent ALMA CO detected galaxies of our sample (solid symbols) and the group-centered galaxies in Werner et al. (2014; open symbols). The CO undetected galaxy NGC 4649 is shown as an upper limit by a solid blue triangle.

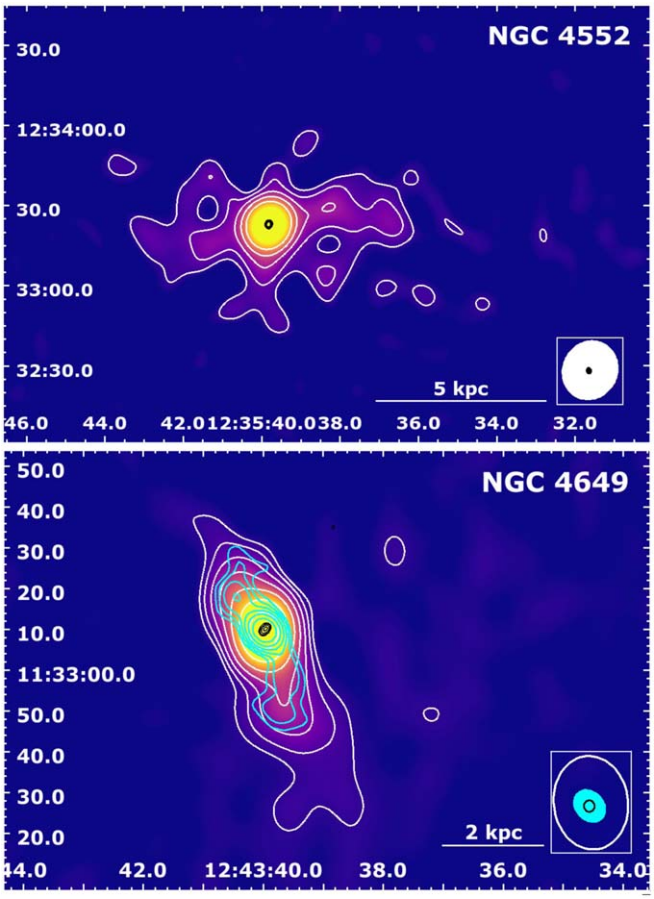

Figure 15. VLA radio total intensity maps at 1–2 GHz for NGC 4552 (top) and NGC 4649 (bottom) in the C and D configurations, respectively. The maps are overlaid by the white contours of these compact configurations; black is for the VLA A configuration, and cyan is for the VLA B configuration contours (previously published by Dunn et al. 2010). In all cases, the contours are created at [1, 2, 4, 8, 16, …] × 5 rms noise and the restoring beams (resolution) are shown in the bottom-right corner of all radio maps (for more details, see Table 5).

predictions from the simulated CCA condensed clouds in ETGs (Gaspari et al. 2017). Such k-plot shows that the observed cool elements are within the expected kinematics from a CCA-feeding cycle, and are also comparable to those observed in several other galaxies (red points). A small deviation is that our sample shows a slightly larger mean in the broadening axis, as we are including galaxies with rotation and AGN outbursts (e.g., NGC 4261), both shown to enhance the k-plot loci toward the upper-right sector (Maccagni et al. 2021). Moreover, our cool gas is often under-resolved (especially with SOFIA), meaning that we are only able to capture larger associations of clouds, rather than single elements, thus shifting the points toward the top region of the more ensemble-like regime, where clouds tend to drift in the macro-scale weather.

Another diagnostics of the top-down multiphase condensation is the C-ratio, i.e., the cooling time divided by the turbulence eddy time, $t_{\rm eddy} = 2\pi r^{2/3} L^{1/3}/\sigma_{v,L}$. Following Gaspari et al. (2018), we compute the injection scale L from either the diameter of the main AGN bubble, whenever available (NGC 4374, NGC 4636, NGC 4261; Finoguenov et al. 2008; Baldi et al. 2009; O'Sullivan et al. 2011), or the extension of the multiphase gas (roughly half the SOFIA beam). To get the macro-scale dispersion $\sigma_{v,L}$, we leverage the SOFIA FOV and average the related cool-gas velocity dispersions detected in each galaxy (Table 6; for NGC 4636, we also include Werner et al. 2014 multiphase gas observations). This is multiplied by $\sqrt{3}$ to account for the 3D kinematics. Figure 17 shows the computed C-ratio for our galaxies with cool gas, superposed to the 99% confidence-level band where significant precipitation is expected to trigger or be present. NGC 4636 has the overall lowest C-ratio, which predicts a condensation rain up to ∼3 kpc, as corroborated by the observed extended multiphase filaments. Although the detection of the core is still missing, NGC 4406 instead has a C-ratio ∼10, suggesting that the rain is very feeble or that the cool gas has originated from a merger (Section 5.1.1). In between, our three other galaxies have a C-ratio that is significantly below the condensation threshold within $r < 1$ kpc; thus, we expect a more localized inner rain, consistent with the relative compact central structures observed in CO and [C II]. This shows how the condensation differs between central (NGC 4636) and noncentral galaxies (the rest of our sample); the former trigger an extended rain, while the latter tend to develop a smaller subkiloparsec weather region (as also predicted via X-ray scaling relations; see Figure 18 in Gaspari et al. 2019).

Figure 18 shows the nuclear radio emission observed at 1–2 GHz taken in several VLA configurations. The sources have a wide range of radio power and morphologies. Table 8 presents the AGN jet power $P_{\rm jet}$, calculated as the work

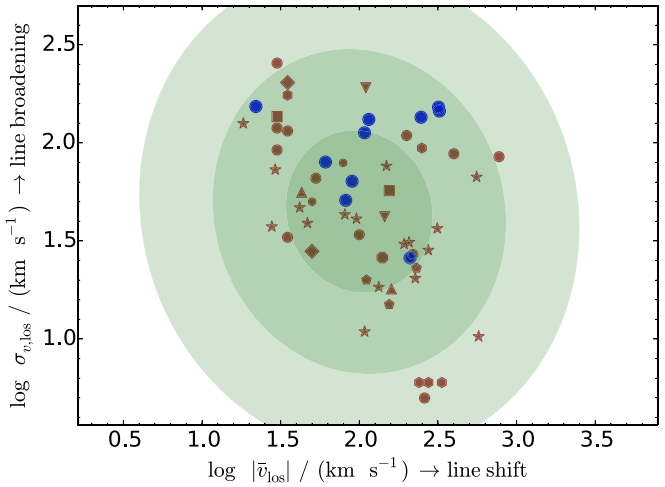

Figure 16. CCA k-plot diagnostic (pencil-beam): line broadening vs. line shift, separating turbulence vs. bulk motions. The red points are the observed cool clouds in massive ETGs from Gaspari et al. (2018; see this paper for more details on the k-plot and their sample). The blue points denote the cool gas detected in our galaxies via [C II] and CO, whenever available (see Table 6; note that $\sigma_v = \mathrm{FWHM}/2.355$). For NGC 4261, we use only the more accurate two-Gaussian "2G" fit. The green shaded contours are the 1σ–3σ confidence level predicted via high-resolution CCA simulations (Gaspari et al. 2017). Our galaxies with cool gas are within the typically expected kinematics from a CCA-feeding cycle.

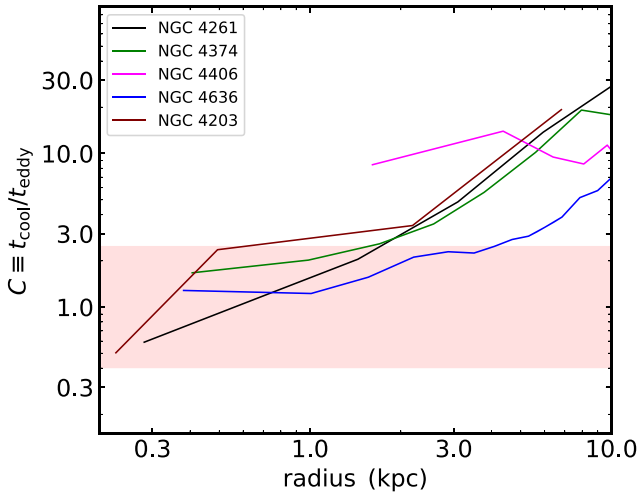

Figure 17. Ratio of the cooling time and turbulence eddy turnover time for our sample of galaxies with cool gas (see the legend and text for more details). The red band shows the 99% confidence level predicted by the CCA simulations (Gaspari et al. 2018) within which significant nonlinear condensation is expected. Most of our noncentral galaxies are expected to develop only an inner rain, at variance with the central NGC 4636 galaxy, which can develop more extended multiphase condensation. Note also how the C-ratio is a more robust indicator of condensation, compared with $t_{\rm cool}/t_{\rm eddy}$, especially in the central regions.

required to inflate a cavity, taken from recent literature. The $P_{\rm jet}$ of the individual galaxies spans a range of two orders of magnitude. The limited data available does not allow for a robust analysis of correlations between the $P_{\rm jet}$ and Hα luminosity or the amount of cold gas. However, the three galaxies with (reliably) detected Hα+[N II] emission (NGC 4204, NGC 4374, and NGC 4636) seem to indicate a positive correlation of jet power with $L_{\rm H\alpha}$. In the scenario of the recursive AGN self-regulation, such a correlation is expected since the SMBH accretion rate increases due to stronger CCA rain, giving rise to larger AGN power, while the cool gas mass increases via top-down condensation (Gaspari et al. 2017, 2018).

The analysis of the radio power and the morphology of the radio emission in each individual galaxy may provide some insights into the AGN feeding/feedback processes. Detailed studies of the very powerful jet in NGC 4261 (O'Sullivan et al. 2011; Kolokythas et al. 2015) suggest that the radio source has gone through multiple AGN outbursts or significant changes in jet power on a timescale of $\sim 10^5$ yr (Worrall et al. 2010). CCA-regulated feedback naturally predicts short AGN bursts for elliptical galaxies, which are proportional to the central cooling time (Gaspari et al. 2019). The related frequent chaotic AGN feeding and feedback cycles are likely responsible for the significant scatter in the cooling time and entropy profiles observed.

The large extent of the radio emission in NGC 4261 indicates that the energy deposition has progressively occurred at larger radii, allowing the cooling to occur at the center. As a result, the hot galactic atmosphere is relatively undisturbed (Figure 11) with fairly regular entropy distribution (Figure 12). Radio observations of NGC 4374 and NGC 4636 show less powerful jets with energy deposited in the central region (NGC 4374) or just outside the radiance core (NGC 4636). Consistently, the X-ray gas shows distinct signs of disturbances generated by central energy deposition via AGN outbursts. Together with the k-plot and C-ratio above, the detection of our galaxies with cool gas overall corroborates the phase of the recursive CCA feeding, in which the increased condensation (in particular within the kiloparsec region) triggers more vigorous AGN heating and activity.

5.1.3. Stellar Mass Loss

It is expected that cold gas originating from the cooling of the hot halo is initially dust poor (e.g., Tsai & Mathews 1995; Valentini & Brighenti 2015). Given the relatively short timescales for the grain sputtering time, $t_{\rm sp} \approx 1.2 \times 10^7 (a/0.1\mu\mathrm{m})(n_e/10^{-2})^{-1}$ yr, where a is the grain radius (Temi et al. 2007b), dust is not expected to survive long-term when in contact with the hot halo. Although dust can grow by accretion of gas-phase metals in the cold gas, it is not clear if the timescale of such a process is compatible with the short sputtering time (e.g., Valentini & Brighenti 2015). Thus, it is possible that some of the observed cool gas may originate from stellar mass loss. Mathews & Brighenti (2003) showed that dusty gas ejected from red giant stars within about 1 kpc of galaxy centers can settle into the core while retaining a significant fraction of its original dust. Dust is protected from sputtering if it remains in warm $T \approx 10^4$ K ionized gas for $\sim 10^6$ yr, which is comparable with the dynamical (freefall) time at $\sim$1 kpc in ellipticals. Alternatively, if this dust immediately goes into the 10^7 K hot gas, it can rapidly cool it to $\sim 10^4$ K in $\lesssim 10^6$ yr by inelastic electron–dust collisions (Mathews & Brighenti 2003).

Previous studies based on the detection of molecular gas in ETGs using the ATLAS and MASSIVE galaxy surveys (Young et al. 2011; Davis et al. 2019) show no correlation between the molecular gas mass and the stellar mass. The molecular gas content in our galactic sample, as shown in Figure 14 and Table 6, covers approximately two orders of

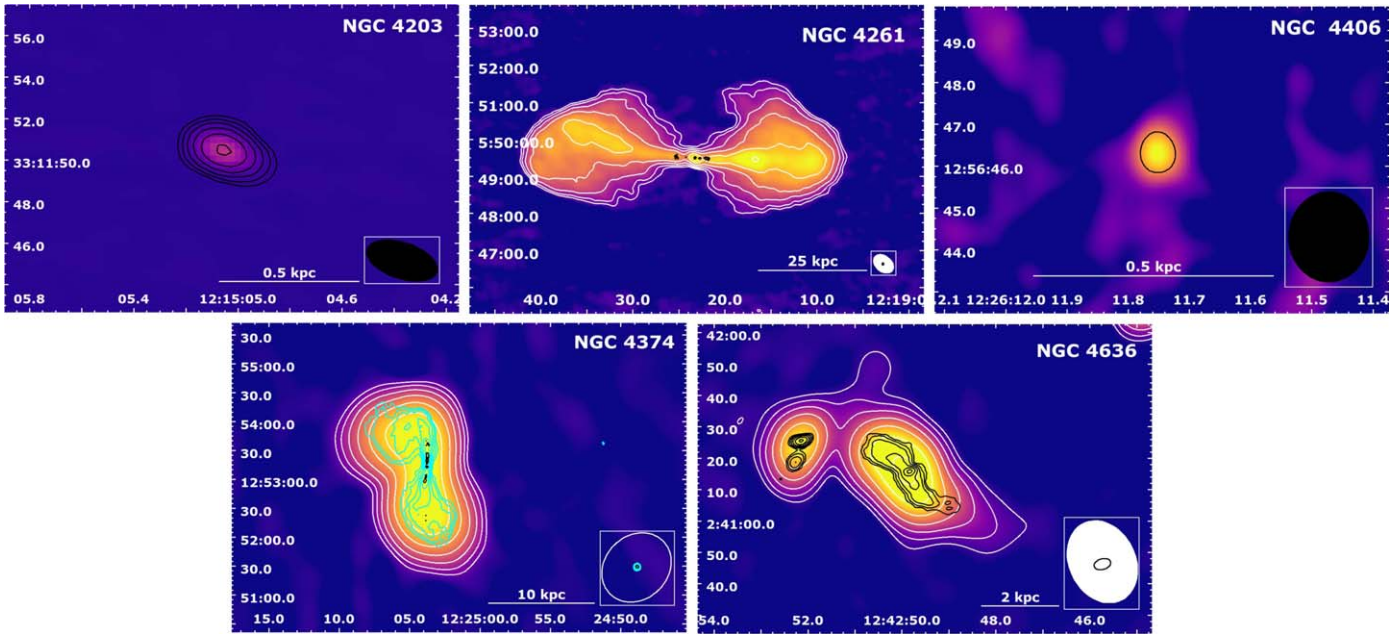

Figure 18. VLA radio total intensity maps at 1–2 GHz for NGC 4203 (top left) and NGC 4406 (top right) in A configuration and NGC 4261 (top middle), NGC 4374 (bottom left), and NGC 4636 (bottom right) in the C configuration. The white radio contours corresponds to the VLA C configuration, the black contours to VLA A configuration, and cyan contours to the VLA B configuration. In all cases, the contours are created at [1, 2, 4, 8, 16,…] × 5 rms noise, and the restoring beams (resolution) are shown in the bottom-right corner of all radio maps (for more details see Table 5).

magnitude, while the L_K luminosity is within a factor of two. Thus, these additional data confirm the lack of dependence of the molecular gas content on the stellar mass, with the implication that stellar mass loss is not the primary source of molecular gas in these galaxies.

6. Conclusions

We have investigated the cold gas content of a sample of six massive elliptical galaxies taken from the sample of 18 nearby ($d < 100$ Mpc), massive, X-ray bright ETGs studied by Dunn et al. (2010). New observations of the 157 μm C II emission line taken with the FIFI-LS instrument on board of SOFIA, along with new ALMA CO observations and radio data from VLA, are presented. These data, complemented with a large multiwavelength data set available in the literature, are used to probe the complex ISM of the galactic sample. The results are compared to previous studies of elliptical galaxies in a parent sample of six galaxies (Werner et al. 2014) extracted from the same original sample of Dunn et al. (2010) and to the investigations of ETGs by the MASSIVE and ATLAS surveys.

We find that the gas/dust evolution in our galaxies (most of which are noncentral galaxies) seems to be driven by a combination of mechanisms, which can alternate during the recent history of the galaxy. Several galaxies are well described by multiphase condensation diagnostics, while a few others (e.g., NGC 4406) display potential merger-like features. The central galaxies studied by Werner et al. (2014) tend instead to be predominantly shaped by internal process, given the rare merger-like interactions. Given the deeper potential wells and larger gas mass, central ellipticals tend to have much lower cooling times ($\propto K^{3/2}$) over extended radii (tens of kiloparsecs). These central galaxies are akin to cool-core systems, which have substantial condensation and AGN activity but on more extended regions. In contrast, our sample of noncentral galaxies does not have such an extended gaseous halo, and as a consequence of lower densities and higher cooling times at large radii, the condensation occurs only within a few kiloparsecs. Overall, our key conclusions are summarized as follows:

1. The small galactic sample shows significant diversity in cold gas content. The [C II] line emission is detected in three out of six galaxies. Complementary multiwavelength data of two galaxies undetected in C II with SOFIA FIFI-LS, NGC4649, and NGC4552, confirm that these systems are devoid of cold gas or a significant amount of dust. The third galaxy with no detection in the carbon line, NGC 4374 (M84), displays instead filamentary Hα+[N II] emission, dust, and molecular gas. Most likely, deeper observations in the 157 μm line may reveal C II emitting gas.
2. The distribution of the detected cool gas phase in our six (noncentral) galaxies is often centrally concentrated and compact, at variance with the cold gas-rich galaxies studied in Werner et al. (2014). Although not large in absolute terms when compared to MASSIVE and ATLAS surveys of ETGs, the cold gas content spans two orders of magnitude among the sample.
3. Although some of the observed cool gas may originate from stellar mass loss, the kinematical and photometric misalignment between cold gas and stars suggest that in these galaxies, stellar mass loss is not the primary source of molecular gas.
4. Given the diversified environment in which some of the galaxies live in, it is conceivable that NGC 4261, NGC 4406, and NGC 4552 may have acquired part of their gas externally via galaxy–galaxy interactions, although we find at best qualitative evidences.
5. Most galaxies in our sample have similar entropy and cooling time profiles, albeit with large scatter. This is at variance with the sample of central massive ETGs studied by Werner et al. (2014), with a dichotomy in the X-ray

properties between cold-gas-rich and -poor systems. Combined with the diversity in the cold-gas content, this argues for a composite origin of their multiphase medium or for a different stage in the AGN feeding/feedback cycle.

6. A few galaxies have active radio jets, which tend to deposit their energy in the large-scale hot atmospheres. Gas cooling is promoted at small radii, while at larger radii, the atmospheres remain single phase (except for NGC 4636), which is consistent with the observed spatial distribution of the cold gas.
7. Comparing with the CCA predictions, we find that our cool gas-free galaxies are likely in the overheated interval of the self-regulated cycle without major signatures of recent AGN activity. For the cool-gas galaxies, the k-plot and AGN power correlation instead corroborate the phase of recursive CCA feeding in which the increased condensation (further enhanced via rotation) is starting to trigger more vigorous AGN heating. The C-ratio consistently shows that central (NGC 4636) and non-central galaxies are expected to generate an extended or inner rain, respectively.

This work is based in part on observations made with the NASA/DLR Stratospheric Observatory for Infrared Astronomy (SOFIA). SOFIA is jointly operated by the Universities Space Research Association, Inc. (USRA), under NASA contract NNA17BF53C, and the Deutsches SOFIA Institut (DSI) under DLR contract 50 OK 0901 to the University of Stuttgart. This paper makes use of the following ALMA data: ADS/JAO. ALMA#2015.1.01107.S, ADS/JAO.ALMA#2017.1.00301.S, and ADS/JAO.ALMA#2017.1.00830.S. The National Radio Astronomy Observatory is a facility of the National Science Foundation operated under cooperative agreement by Associated Universities, Inc. HPC resources were provided by the NASA High-End Computing (HEC) Program (SMD-1153) through the NASA Advanced Supercomputing (NAS) Division at Ames Research Center. M.G. acknowledges partial support by NASA Chandra GO9-20114X and HST GO-15890.020/023-A, and the BlackHoleWeather program. N.W. and R.G. are supported by the GACR grant 21-13491X. R.G. thanks Elisabetta Liuzzo for supervision and guidance with ALMA data reduction. A.S. is supported by the Women In Science Excel (WISE) program of the Netherlands Organisation for Scientific Research (NWO), and acknowledges the World Premier Research Center Initiative (WPI) and the Kavli IPMU for the continued hospitality. SRON Netherlands Institute for Space Research is supported financially by NWO.

Software: CASA (v4.7.2, McMullin et al. 2007), ZAP (Soto et al. 2016), CIGALEMC (Serra et al. 2011) MAGPHYS14 (Da Cunha et al. 2008), XSPEC (Arnaud 1996), SPEX (Kaastra et al. 1996), scikit-learn (Pedregosa et al. 2011), GALFIT (Peng et al. 2010), photutils (Bradley et al. 2019).

ORCID iDs

P. Temi https://orcid.org/0000-0002-8341-342X
M. Gaspari https://orcid.org/0000-0003-2754-9258
F. Brighenti https://orcid.org/0000-0001-9807-8479
N. Werner https://orcid.org/0000-0003-0392-0120
R. Grossova https://orcid.org/0000-0003-3471-7459
M. Gitti https://orcid.org/0000-0002-0843-3009
M. Sun https://orcid.org/0000-0001-5880-0703
A. Simionescu https://orcid.org/0000-0002-9714-3862

References

Allen, S. W., Dunn, R. J. H., Fabian, A. C., et al. 2006, MNRAS, 372, 21
Amblard, A., Riguccini, L., Temi, P., et al. 2014, ApJ, 783, 135
Arnaud, K. A. 1996, in ASP Conf. Ser. 101, Astronomical Data Analysis Software and Systems V, ed. G. H. Jacoby & J. Barnes (San Francisco, CA: ASP), 17
Babyk, I. V., McNamara, B. R., Tamhane, P. D., et al. 2019, ApJ, 887, 149
Baldi, A., Forman, W., Jones, C., et al. 2009, ApJ, 707, 1034
Beuing, J., Dobereiner, S., Bohringer, H., & Bender, R. 1999, MNRAS, 302, 209
Birkinshaw, M., & Davies, R. L. 1985, ApJ, 291, 32
Boizelle, B. D., Barth, A. J., Darling, J., et al. 2017, ApJ, 845, 170
Boizelle, B. D., Walsh, J. L., Barth, A., et al. 2021, ApJ, 908, 19
Bolatto, A. D., Wolfire, M., & Leroy, A. K. 2013, ARA&A, 51, 207
Boselli, A., Fossati, M., Longobardi, A., et al. 2022, A&A, 659, A46
Bower, R. G., Benson, A. J., Malbon, R., et al. 2006, MNRAS, 370, 645
Bradley, L., Sipocz, B., Robitaille, T., et al. 2019, astropy/photutils: v0.6, Zenodo, https://doi.org/10.5281/zenodo.2533376
Briggs, D. S. 1995, BAAS, 27, 1444
Brighenti, F., & Mathews, W. G. 1996, ApJ, 470, 747
Brighenti, F., Mathews, W. G., & Temi, P. 2015, ApJ, 802, 118
Canning, R. E. A., Ferland, G. J., Fabian, A. C., et al. 2016, MNRAS, 455, 3042
Caon, N., Macchetto, D., & Pastoriza, M. 2000, ApJS, 127, 39
Cappellari, M., Emsellem, E., Krajnović, D., et al. 2011, MNRAS, 413, 813
Ciesla, L., Boselli, A., Smith, M. W. L., et al. 2012, A&A, 543, A161
Combes, F., Young, L. M., & Bureau, M. 2007, MNRAS, 377, 1795
Cortese, L., Fritz, J., Bianchi, S., et al. 2014, MNRAS, 440, 942
Croton, D. J., Springel, V., White, S. D. M., et al. 2006, MNRAS, 365, 11
Da Cunha, E., Charlot, S., & Elbaz, D. 2008, MNRAS, 388, 1595
D'Abrusco, R., Fabbiano, G., Mineo, S., et al. 2014, ApJ, 783, 18
David, L. P., Lim, J., Forman, W., et al. 2014, ApJ, 792, 94
Davis, T. A., Alatalo, K., Sarzi, M., et al. 2011, MNRAS, 417, 882
Davis, T. A., Greene, J. E., Ma, C.-P., et al. 2019, MNRAS, 486, 1404
Dunn, R. J. H., Allen, S. W., Taylor, G. B., et al. 2010, MNRAS, 404, 180
Emsellem, E., Cappellari, M., Krajnović, D., et al. 2011, MNRAS, 414, 888
Fabbiano, G., Kim, D. W., & Trinchieri, G. 1992, ApJS, 80, 531
Finoguenov, A., & Jones, C. 2001, ApJL, 547, L107
Finoguenov, A., Ruszkowski, M., Jones, C., et al. 2008, ApJ, 686, 911
Fischer, C., Beckmann, S., Bryant, A., et al. 2018, JAI, 7, 1840003
Fossati, M., Fumagalli, M., Boselli, A., et al. 2016, MNRAS, 455, 2028
Foster, A. R., Ji, L., Smith, R. K., & Brickhouse, N. S. 2012, ApJ, 756, 128
Gaspari, M., Brighenti, F., & Temi, P. 2012, MNRAS, 424, 190
Gaspari, M., Brighenti, F., & Temi, P. 2015, A&A, 579, A62
Gaspari, M., McDonald, M., Hamer, S. L., et al. 2018, ApJ, 854, 167
Gaspari, M., Ruszkowski, M., & Oh, S. P. 2013, MNRAS, 432, 3401
Gaspari, M., Temi, P., & Brighenti, F. 2017, MNRAS, 466, 677
Gaspari, M., Tombesi, F., & Cappi, M. 2020, NatAs, 4, 10
Gaspari, M., Eckert, D., Ittori, S., et al. 2019, ApJ, 884, 169
Gavazzi, G., Consolandi, G., Pedraglio, S., et al. 2018, A&A, 611, A28
Gomez, H. L., Baes, M., Cortese, L., et al. 2010, A&A, 518, L45
Griffin, M. J., Abergel, A., Abreu, A., et al. 2010, A&A, 518, L3
Grossová, R., Werner, N., Rajpurohit, K., et al. 2019, MNRAS, 488, 1917
Ho, L. C., Filippenko, A. V., & Sargent, W. L. W. 1997, ApJS, 112, 315
Humphrey, P. J., Buote, D. A., Brighenti, F., et al. 2013, MNRAS, 430, 1516
Humphrey, P. J., Buote, D. A., Brighenti, F., Gebhardt, K., & Mathews, W. G. 2008, ApJ, 683, 161
Jaffe, W., Ford, H. C., Ferrarese, L., et al. 1993, Natur, 364, 213
Juráňová, A., Werner, N., Gaspari, M., et al. 2019, MNRAS, 484, 2886
Juráňová, A., Werner, N., Nulsen, P. E. J., et al. 2020, MNRAS, 499, 5163
Kaastra, J. S., Mewe, R., & Nieuwenhuijzen, H. 1996, 11th Colloquium on UV and X-ray Spectroscopy of Astrophysical and Laboratory Plasmas (Nagoya, Japan), 411
Kalberla, P. M. W., Burton, W. B., Hartmann, D., et al. 2005, A&A, 440, 775
Kaviraj, S., Schawinski, K., Devriendt, J. E. G., et al. 2007, ApJS, 173, 619
Kenney, J. D. P., Tal, T., Crowl, H. H., et al. 2008, ApJL, 687, L69
King, A., & Pounds, K. 2015, ARA&A, 53, 115
Klein, R., Beckmann, S., Bryant, A., et al. 2014, Proc. SPIE, 9147, 91472X
Kolokythas, K., O'Sullivan, E., Giacintucci, S., et al. 2015, MNRAS, 450, 1732
Kolokythas, K., O'Sullivan, E., Raychaudhury, S., et al. 2018, MNRAS, 481, 1550
Lagos, C. d. P., Davis, T. A., Lacey, C. G., et al. 2014, MNRAS, 443, 1002
Lakhchaura, K., Werner, N., Sun, M., et al. 2018, MNRAS, 481, 4472

Langer, W. D., Velusamy, T., Pineda, J. L., et al. 2014, A&A, 561, A122
Lanz, L., Zezas, A., Brassington, N., et al. 2013, ApJ, 768, 90
Li, Y., Bryan, G. L., Ruszkowski, M., et al. 2015, ApJ, 811, 73
Maccagni, F. M., Serra, P., Gaspari, M., et al. 2021, A&A, 656, A45
Macchetto, F., Pastoriza, M., Caon, N., et al. 1996, A&AS, 120, 463
Machacek, M., Jones, C., Forman, W. R., et al. 2006a, ApJ, 644, 155
Machacek, M., Nulsen, P. E. J., Jones, C., et al. 2006b, ApJ, 648, 947
Mathews, W. G., & Brighenti, F. 1999, ApJ, 526, 114
Mathews, W. G., & Brighenti, F. 2003, ApJL, 590, L5
McMullin, J. P., Waters, B., Schiebel, D., Young, W., & Golap, K. 2007, in ASP Conf. Ser. 376, Astronomical Data Analysis Software and Systems XVI, ed. R. A. Shaw, F. Hill, & D. J. Bell (San Francisco, CA: ASP), 127
McNamara, B. R., & Nulsen, P. E. J. 2007, ARA&A, 45, 117
Nolthenius, R. 1993, ApJS, 85, 1
North, E. V., Davis, T. A., Bureau, M., et al. 2021, MNRAS, 503, 5179
O'Sullivan, E., Worrall, D. M., Birkinshaw, M., et al. 2011, MNRAS, 416, 2916
Pabst, C. H. M., Goicoechea, J. R., Teyssier, D., et al. 2017, A&A, 606, A29
Paggi, A., Kim, D.-W., Anderson, C., et al. 2017, ApJ, 844, 5
Pedregosa, F., Varoquaux, G., & Gramfort, A. 2011, JMLR, 12, 2825
Peng, C. Y., Ho, L. C., Impey, C. D., et al. 2010, AJ, 139, 2097
Perley, R. A., & Butler, B. J. 2013, ApJS, 204, 19
Pineda, J. L., Langer, W. D., Velusamy, T., et al. 2013, A&A, 554, A103
Randall, S., Nulsen, P., Forman, W. R., et al. 2008, ApJ, 688, 208
Rau, U., & Cornwell, T. J. 2011, A&A, 532, A71
Rieke, G. H., Young, E. T., Engelbracht, C. W., et al. 2004, ApJS, 154, 25
Röllig, M., Ossenkopf, V., Jeyakumar, S., et al. 2006, A&A, 451, 917
Rose, T., Edge, A. C., Combes, F., et al. 2019, MNRAS, 489, 349
Ruffa, I., Davis, T. A., Prandoni, I., et al. 2019b, MNRAS, 489, 3739
Ruffa, I., Prandoni, I., Laing, R. A., et al. 2019a, MNRAS, 484, 4239
Sabater, J., Best, P. N., & Argudo-Fernández, M. 2013, MNRAS, 430, 638
Sanders, J. S. 2006, MNRAS, 371, 829
Sarzi, M., Alatalo, K., Blitz, L., et al. 2013, MNRAS, 432, 1845
Serra, P., Amblard, A., Temi, P., et al. 2011, ApJ, 740, 22
Sharma, P., McCourt, M., Quataert, E., et al. 2012, MNRAS, 420, 3174
Sheen, Y.-K., Yi, S. K., Ree, C. H., et al. 2016, ApJ, 827, 32
Shurkin, K., Dunn, R. J. H., Gentile, G., et al. 2008, MNRAS, 383, 923
Smith, R. K., Brickhouse, N. S., Liedahl, D. A., & Raymond, J. C. 2001, ApJ, 556, L91
Soto, K. T., Lilly, S. J., Bacon, R., et al. 2016, MNRAS, 458, 3210
Temi, P., Amblard, A., Gitti, M., et al. 2018, ApJ, 858, 17
Temi, P., Marcum, P. M., Young, E., et al. 2014, ApJS, 212, 24
Temi, P., Brighenti, F., Mathews, W. G., et al. 2004, ApJS, 151, 237
Temi, P., Brighenti, F., & Mathews, W. G. 2005, ApJL, 635, L25
Temi, P., Brighenti, F., & Mathews, W. G. 2007a, ApJ, 660, 1215
Temi, P., Brighenti, F., & Mathews, W. G. 2007b, ApJ, 666, 222
Temi, P., Brighenti, F., & Mathews, W. G. 2009, ApJ, 707, 890
Tonry, J. L., Dressler, A., Blakeslee, J. P., et al. 2001, ApJ, 546, 681
Trinchieri, G., & di Serego Alighieri, S. 1991, AJ, 101, 1647
Tsai, J. C., & Mathews, W. G. 1995, ApJ, 448, 84
Valentini, M., & Brighenti, F. 2015, MNRAS, 448, 1979
Vila-Vilaró, B., Cepa, J., & Butner, H. M. 2003, ApJ, 594, 232
Voit, G. M., Bryan, G. L., O'Shea, B. W., et al. 2015, ApJL, 808, L30
Walsh, J. L., Barth, A. J., & Sarzi, M. 2010, ApJ, 721, 762
Welch, G. A., & Sage, L. J. 2003, ApJ, 584, 260
Werner, N., Allen, S. W., & Simionescu, A. 2012, MNRAS, 425, 2731
Werner, N., Oonk, J. B. R., Sun, M., et al. 2014, MNRAS, 439, 2291
Wiklind, T., Combes, F., & Henkel, C. 1995, A&A, 297, 643
Wittor, D., & Gaspari, M. 2020, MNRAS, 498, 4983
Wolfire, M. G., Hollenbach, D., & Tielens, A. G. G. M. 1989, ApJ, 344, 770
Wood, R. A., Jones, C., Machacek, M. E., Forman, W. R., et al. 2017, ApJ, 847, 79
Worrall, D. M., Birkinshaw, M., O'Sullivan, E., et al. 2010, MNRAS, 408, 701
Yang, H. Y. K., Gaspari, M., & Marlow, C. 2019, ApJ, 871, 6
Yıldız, M. K., Serra, P., Peletier, R. F., Oosterloo, T. A., & Duc, P.-A. 2017, MNRAS, 464, 329
Young, E. T., Becklin, E. E., Marcum, P. M., et al. 2012, ApJL, 749, L17
Young, L. M., Bureau, M., Davis, T. A., et al. 2011, MNRAS, 414, 940